Article

Structure

Crystal Structure and Conformational Change Mechanism of a Bacterial Nramp-Family Divalent Metal Transporter

Graphical Abstract

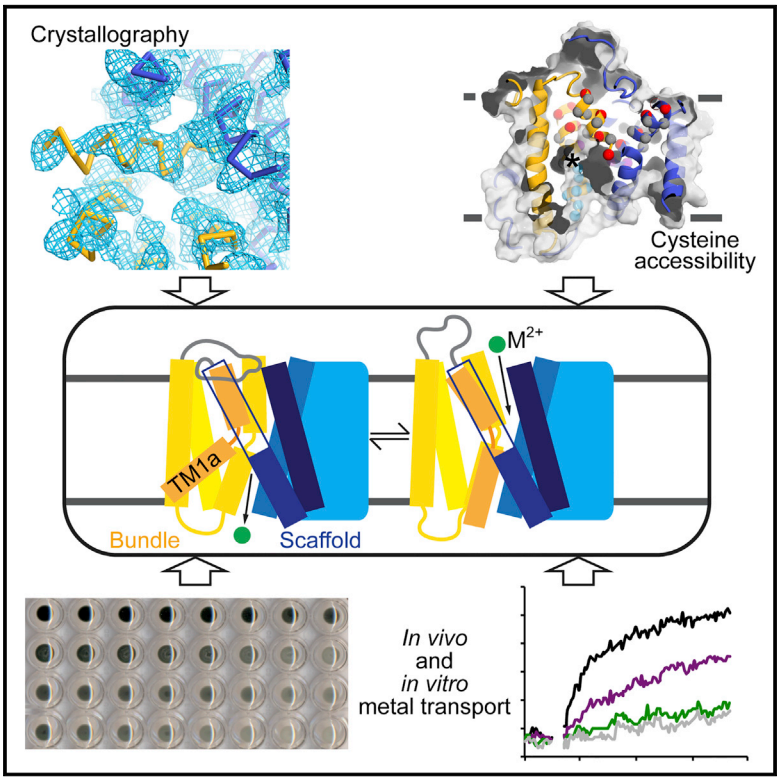

Authors

Aaron T. Bozzi, Lukas B. Bane, Wilhelm A. Weihofen, ..., Hidde L. Ploegh, Klaus Schulten, Rachelle Gaudet

Correspondence

gaudet@mcb.harvard.edu

In Brief

Bozzi et al. determined the inward-open structure of a bacterial Nramp transition metal transporter with a LeuT fold. Using biochemical experiments, the authors provide mechanistic explanations for how two anemia-causing mutations impede function through altering the conformational landscape of the protein in unique ways.

Highlights

- *Deinococcus radiodurans* Nramp structure reveals TM1a location in inward-open state
- Unfettered movement of TM1a is essential to the metal-transport cycle
- G153R disease-mutant mimic alters selectivity of conserved metal-binding site
- G45R disease-mutant mimic sterically locks protein in inward-open state

Accession Numbers

5KTE

Bozzi et al., 2016, Structure *24*, 1–13
December 6, 2016
http://dx.doi.org/10.1016/j.str.2016.09.017

CellPress

Please cite this article in press as: Bozzi et al., Crystal Structure and Conformational Change Mechanism of a Bacterial Nramp-Family Divalent Metal Transporter, Structure (2016), http://dx.doi.org/10.1016/j.str.2016.09.017

Structure
Article

Crystal Structure and Conformational Change Mechanism of a Bacterial Nramp-Family Divalent Metal Transporter

Aaron T. Bozzi,[1,5] Lukas B. Bane,[1,5,6] Wilhelm A. Weihofen,[1,5,7] Abhishek Singharoy,[2] Eduardo R. Guillen,[4,8] Hidde L. Ploegh,[4] Klaus Schulten,[2,3] and Rachelle Gaudet[1,9,*]
[1]Department of Molecular and Cellular Biology, Harvard University, 52 Oxford Street, Cambridge, MA 02138, USA
[2]Beckman Institute for Advanced Science and Technology
[3]Department of Physics
University of Illinois at Urbana-Champaign, Urbana, IL 61801, USA
[4]Whitehead Institute for Biomedical Research, Nine Cambridge Center, Cambridge, MA 02142, USA
[5]Co-first author
[6]Present address: D.E. Shaw Research, New York, NY 10036, USA
[7]Present address: Novartis Institutes for Biomedical Research, Cambridge, MA 02139, USA
[8]Present address: EpiVax, Inc, 146 Clifford Street, Providence, RI 02903, USA
[9]Lead Contact
*Correspondence: gaudet@mcb.harvard.edu
http://dx.doi.org/10.1016/j.str.2016.09.017

SUMMARY

The widely conserved natural resistance-associated macrophage protein (Nramp) family of divalent metal transporters enables manganese import in bacteria and dietary iron uptake in mammals. We determined the crystal structure of the *Deinococcus radiodurans* Nramp homolog (DraNramp) in an inward-facing apo state, including the complete transmembrane (TM) segment 1a (absent from a previous Nramp structure). Mapping our cysteine accessibility scanning results onto this structure, we identified the metal-permeation pathway in the alternate outward-open conformation. We investigated the functional impact of two natural anemia-causing glycine-to-arginine mutations that impaired transition metal transport in both human Nramp2 and DraNramp. The TM4 G153R mutation perturbs the closing of the outward metal-permeation pathway and alters the selectivity of the conserved metal-binding site. In contrast, the TM1a G45R mutation prevents conformational change by sterically blocking the essential movement of that helix, thus locking the transporter in an inward-facing state.

INTRODUCTION

Nearly all organisms require iron to survive. The oxidation state cycle of iron is ideal both to catalyze essential redox reactions as a co-factor in numerous enzymes and to provide a pathway for electron transport across membranes. In addition, heme iron is used for oxygen transport and storage, enabling aerobic respiration. Organisms have thus evolved mechanisms to acquire, traffic, and safely store this crucial transition metal (Aisen et al., 2001; Andrews, 2008). The natural resistance-associated macrophage protein (Nramp) family of divalent metal transporters plays a vital role in mammalian iron homeostasis (Mackenzie and Hediger, 2004). Expressed in phagosomal membranes, Nramp1 both helps macrophages kill engulfed pathogens by extracting iron and other essential transition metals (Cellier et al., 2007), and enables iron recycling from dying erythrocytes (Soe-Lin et al., 2009). Mammals abundantly express a second homolog, Nramp2 (also known as divalent metal transporter 1) in intestinal enterocytes to enable absorption of dietary iron (Gunshin et al., 1997). Nramp2 is also expressed at lower levels in the endosomal membranes of most somatic cells (Mackenzie et al., 2007), where it enables extraction of transferrin-bound iron from vesicles, an especially important process in erythropoiesis (Canonne-Hergaux et al., 2001; Gunshin et al., 2005).

To maintain homeostasis, mammals tightly regulate iron uptake and transport (Lieu et al., 2001), primarily through translation and localization of Nramps (Gunshin et al., 2001; Hubert and Hentze, 2002). An overabundance of free iron generates free radicals that cause tissue damage and increase susceptibility to infection (Ganz, 2009). In contrast, iron deficiency causes anemia (Abbaspour et al., 2014). Accordingly, mutations in Nramp2 are implicated in anemia in humans and rodents (Iolascon and De Falco, 2009; Shawki et al., 2012). The same glycine-to-arginine mutation (G185R) causes microcytic anemia in both mice (Fleming et al., 1997) and Belgrade rats (Fleming et al., 1998; Veuthey and Wessling-Resnick, 2014), and altered protein localization in enterocytes (Canonne-Hergaux et al., 2000). This mutation reduces iron transport when expressed in mammalian cell lines (Su et al., 1998; Touret et al., 2004; Xu et al., 2004), with a concomitant increase in permeability to calcium (typically a poor Nramp substrate) in G185R-transfected cells compared with wild-type (WT) counterparts (Xu et al., 2004). A glycine-to-arginine mutation (G75R) in human anemia patients may abrogate iron transport function (Barrios et al., 2012; Blanco et al., 2009; Shawki et al., 2012). However, the molecular mechanisms

Table 1. Data Collection and Refinement Statistics

	Fab	DraNramp
PDB	NA	5KTE
SBGrid Databank	335	332, 333, 334
Data Collection		
Wavelength (Å)	0.97917	1.139
Resolution range (Å)	30.00–3.00 (3.11–3.00)	46.47–3.94 (4.08–3.94)
Space group	$P2_12_12_1$	I222
Unit cell (a, b, c)	116.17, 183.66, 299.88	113.13, 132.08, 221.0
No. of crystals	1	3
Total reflections	558,353	245,867
Unique reflections	119,718	11,791 (462)
Redundancy	4.7 (4.8)	16.6 (11.4)
Completeness (%)	99.5 (100.0)	95 (96)
Mean I/σ(I)	8.4 (2.2)	6 (.61)
R_{merge}	0.151	0.171
R_{meas}		0.177
R_{pim}		0.047
$CC_{1/2}$		0.99 (0.189)
Refinement		
Resolution range (Å)		46.47–3.94 (4.12–3.94)
R_{work}		0.2666 (0.2672)
R_{free}		0.3128 (0.3656)
No. of atoms		5,625
Protein		5,622
Ions (Os)		3
Protein residues		762
Ramachandran plot (%)		
Favored		692 (90.8)
Allowed		66 (8.7)
Outliers		4 (0.52)
RMSD (bonds)		0.005
RMSD (angles)		1.12
Average B factor		89.8
Protein		89.8
Ions (Os)		190

NA, not applicable; RMSD, root-mean-square deviation.

by which these mutations perturb Nramp metal transport and cause anemia remain unknown.

The Nramp family spans the tree of life, with homologs that perform a range of essential divalent transition metal-transport functions, likely as secondary transporters that harness a proton gradient (Courville et al., 2006). Based on sequence analyses, Nramp homologs form four major phylogenetic clades: the eukaryotic Nramps and the prokaryotic A, B, and C clades (Cellier et al., 2001). The crystal structure of *Staphylococcus capitis* Nramp (ScaNramp), belonging to clade C, confirmed a LeuT fold (named for the bacterial sodium/amino acid symporter [Yamashita et al., 2005]) for Nramps, as predicted previously (Cellier, 2012; Ehrnstorfer et al., 2014).

Because of the alternating access model for membrane transport proteins (Jardetzky, 1966), Nramps should cycle between at least two stable conformations: outward-facing to bind its metal substrate, and inward-facing to release its cargo into the cytosol. The ScaNramp structure, in an inward-facing state, revealed a metal-binding site that consists of conserved aspartate, asparagine, and methionine residues, and a backbone carbonyl from transmembrane segments (TMs) 1 and 6 that coordinate a range of divalent metal substrates (Ehrnstorfer et al., 2014), with the methionine providing a selective preference for transition metals over alkaline earth metals (Bozzi et al., 2016).

Here we present the crystal structure of the *Deinococcus radiodurans* Nramp homolog (DraNramp) from prokaryotic clade A. The DraNramp structure represents an inward-facing apo conformation, with TM1a, absent from the ScaNramp crystallization construct, swung up to open a large intracellular vestibule. We use this structure along with extensive cysteine accessibility and metal-transport measurements to propose a model for conformational change in this LeuT-fold transporter and explain the mechanistic effects of two anemia-causing mammalian Nramp2 mutations. In our model, reaching the outward-facing state requires TM1a to approach the protein core to close the intracellular vestibule. This motion is prevented by an N-terminal glycine-to-arginine mutation that mimics an anemia-causing mutation in human Nramp2. The second disease-mimicking glycine-to-arginine mutation alters the extracellular vestibule and metal-binding site, resulting in reduced transport activity and altered selectivity.

RESULTS

The DraNramp Inward-Facing Structure Shows a Highly Kinked Transmembrane Helix 1

We determined the crystal structure of detergent-solubilized DraNramp (38% sequence identity with ScaNramp) in complex with a monoclonal antibody fragment (Fab) to 3.9-Å resolution (Table 1). Crystallization was facilitated by intracellular surface mutations (Figure 1B; see below). We used a ScaNramp-based homology model and the Fab fragment crystal structure as molecular replacement (MR) search models, with additional phasing provided by single-wavelength anomalous signals from three osmium ions bound to the Fab or at crystal contacts (Figure S1). Refinement was facilitated by using xMDFF (McGreevy et al., 2014; Singharoy et al., 2015). In particular, we used a combination of xMDFF and steered molecular dynamics to optimize our TM1a model, exploring different TM1a positional registries corresponding to a screw axis rotation of approximately one helical turn. The assigned TM1a registry (Figure 1D) yielded both the lowest R factor and the best agreement with cysteine accessibility data (see Figures 6 and 7; see below). The final asymmetric unit comprises one DraNramp transporter, one Fab bound to the DraNramp periplasmic face, and three osmium ions, with crystal-packing interactions between the Fab and the DraNramp cytoplasmic face (Figure S1). All 11 DraNramp TMs are visible in the electron density, including TM1a, which was truncated in ScaNramp (Ehrnstorfer et al., 2014).

Like ScaNramp, DraNramp has a LeuT fold with two pseudosymmetry-related structural repeats comprising TMs 1–5

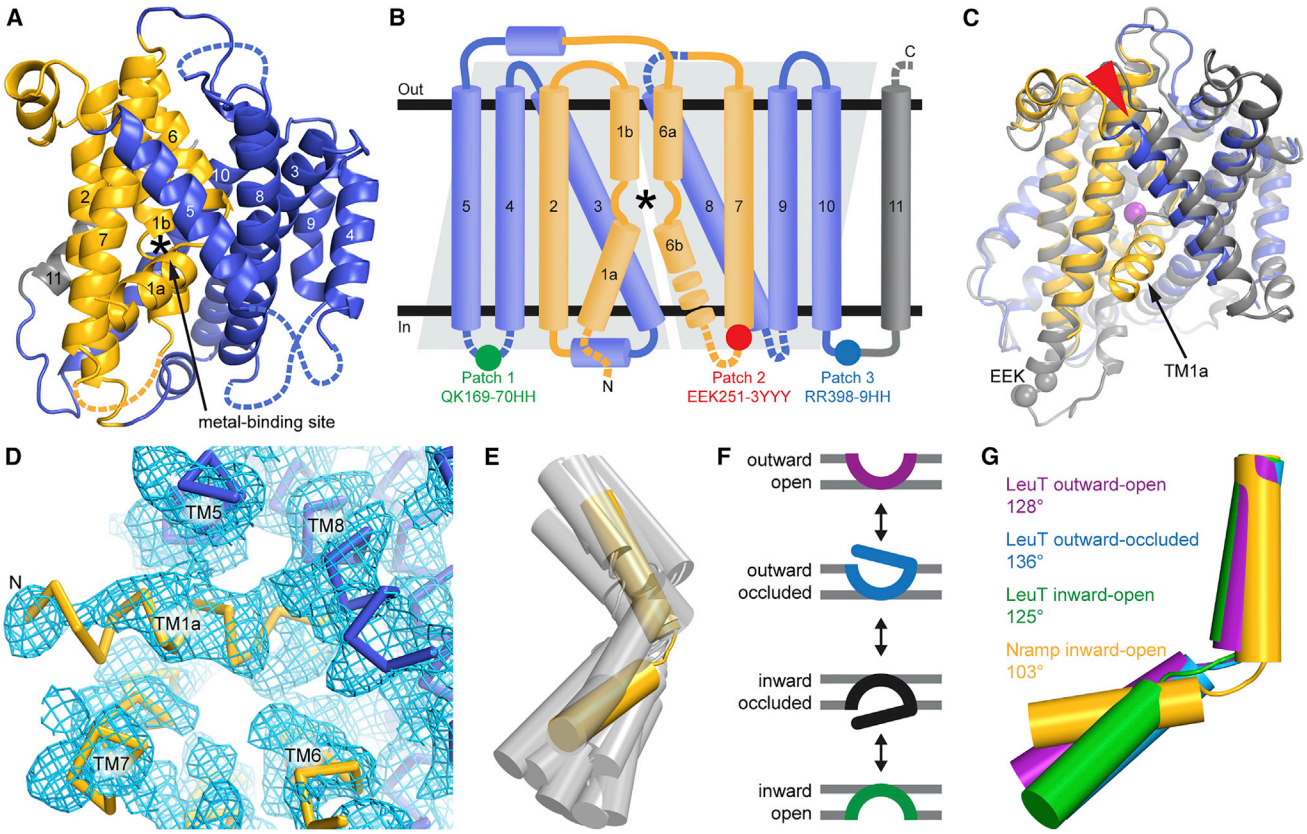

Figure 1. DraNramp Structure in the Inward-Facing State Shows a Highly Kinked TM1

(A) Cartoon representation of DraNramp with TM helices labeled; the bundle (TMs 1, 2, 6, and 7) is gold, scaffold (TMs 3, 4, 5, 8, 9, and 10) blue, and TM11 gray. Dashed loops are disordered in the structure. (B) DraNramp topology diagram, with helices as cylinders, and gray trapezoids highlighting the inverted structural repeats (TMs 1–5 and TMs 6–10). Intracellular loop mutations patch 1 to 3 in the crystallized construct are indicated.

(C) Superposition of DraNramp (blue and gold) and ScaNramp (PDB: 4WGW; gray and Mn^{2+} magenta) indicates a similar overall fold. The main differences are the position of TM5 (red arrowhead) and the presence of TM1a in DraNramp. Gray spheres mark the ScaNramp EEK motif corresponding to patch 2, disordered in DraNramp.

(D) Final $2F_o - F_c$ electron density map at 0.8 σ showing density for TM1a. DraNramp is represented as a Cα trace.

(E) Comparison of TM1 kink angle of DraNramp (yellow) with published LeuT-fold structures (gray; LeuT PDB: 2A65, 3TT1, 3TT3, 5JAE; Mhp1 PDB: 2JLN, 4D1B, 2X79; vSGLT PDB: 2XQ2, 3DH4; BetP PDB: 4LLH, 4AIN, 4DOJ, 4C7R). The scaffolds of the corresponding structures were superimposed and oriented as in (A).

(F) Conformational states in a transport cycle, color coded as in (G).

(G) The TM1b helices were aligned for DraNramp and three distinct LeuT conformations, highlighting the common kink at the unwound substrate-binding region in the middle of TM1. The kink is even more pronounced in inward-open DraNramp than any LeuT structure.

See also Figure S1.

and TMs 6–10, respectively (Figures 1A and 1B) (Yamashita et al., 2005). As in other LeuT folds, TMs 1, 2, 6, and 7 form a "rocking bundle" whose putative movements relative to the "scaffold," made up of the remaining TMs, likely effects the switch in active site accessibility from extracellular to intracellular (Forrest and Rudnick, 2009). TM1 and 6 are unwound in the center of the membrane plane, providing substrate-binding residues as observed in ScaNramp (Ehrnstorfer et al., 2014). In DraNramp, the metal-binding site is unoccupied and exposed to the intracellular side (see Figure 2A). Thus the structure represents a substrate-free inward-facing conformation. Accordingly, DraNramp and ScaNramp superimpose well with a root-mean-square distance of 1.54 Å over 279 Cα atoms. Clade A members such as DraNramp have a four-residue deletion near the TM9 N terminus in comparison with clade C members such as ScaNramp, resulting in a shorter helix (Figure S1D) (Cellier, 2012). The main difference between the two structures is the position of scaffold helix TM5 (Figure 1C), more angled relative to the membrane plane in DraNramp, perhaps influenced by the presence of TM1a in the structure.

As in other LeuT-fold proteins (Figure 1E), DraNramp TM1a is bent outward and lies nearly parallel to the membrane between the pillars of scaffold helix TM5 and bundle helix TM7, creating a large aqueous vestibule on the cytoplasmic side of the transporter. The angle between TM1a and 1b is 103°, smaller than that observed in the inward-facing LeuT structure (125°; Krishnamurthy and Gouaux, 2012), and outward-occluded LeuT (136°; Yamashita et al., 2005) (Figures 1F and 1G). Correspondingly this deep bend in TM1 yields a larger vestibule than in LeuT, which could facilitate water coordination of transported metal ions.

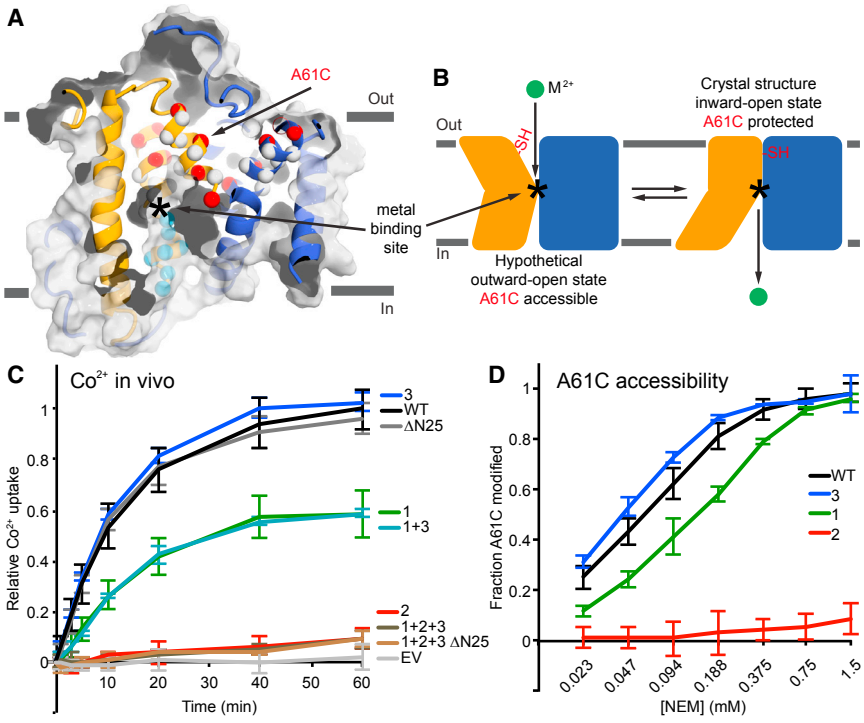

Figure 2. Cysteine Accessibility Scanning Reveals the Outward Metal-Permeation Pathway that Is Sealed Shut in the Crystallized Construct

(A) Internal slice of the inward-facing DraNramp structure, including solvent accessibility of a panel of cysteine mutants spanning TM1, 3, and 6 using NEM. Spheres show Cα positions of highly NEM-protected (gray), outward-accessible (also MTSET and MTSEA-modified; red), inward-accessible (also MTSEA- but not MTSET-modified; cyan), or only NEM-accessible (black) residues. Accessibility is assessed as >50% NEM modification in at least two separate experiments. Many outward-accessible residues, including A61C, are buried in our inward-open structure, suggesting they line an aqueous passage to the metal-binding site (approximate location labeled *) in an alternate outward-open conformation.

(B) The proposed conformational equilibrium of DraNramp, in which A61C is solvent-accessible in the outward-open state, but buried (and thus NEM-protected) in the inward-open conformation.

(C) The patch mutants in the crystallized DraNramp construct, tested alone or in combinations, have varying effects on in vivo Co^{2+} transport. While the 25-residue N-terminal truncation and patch 3 (RR398-9HH) did not impair function, patch 1 (QK169-70HH) reduced transport and patch 2 (EEK251-3YYY) completely eliminated transport.

(D) While the transport-competent patch 1 and 3 mutants retained A61C accessibility (patch 1 at a reduced level), the transport-dead patch 2 mutant eliminated A61C accessibility, suggesting it locks the protein in the inward-open state.

All data are averages ± SD ($n \geq 3$). For reference, WT and empty vector/vesicle (EV) Co^{2+} uptake time course and WT A61C accessibility data are repeated in subsequent figures. See also Figure S2 and Table S1.

Cysteine Accessibility Scanning Reveals an Outward-Facing Metal-Permeation Pathway

To identify a metal-permeation pathway, we created a panel of sequential single-cysteine mutants spanning DraNramp TM1, 3, and 6, which typically line the inward- and/or outward-facing permeation pathway in LeuT-fold transporters (Shi, 2013). The mutations were introduced in the C382S background, which removed the lone endogenous cysteine while retaining full activity (Figure S2E). We measured in vivo accessibility to thiol-specific modifier N-ethylmaleimide (NEM) or inner membrane-impermeable 2-(trimethylammonium)ethyl methane thiosulfonate bromide (MTSET) (Figures S2A and S2B), which both specifically react with aqueous-exposed cysteines (Kaback et al., 2007; Karlin and Akabas, 1998). We classified the cysteine positions in three groups: (1) NEM- and MTSET-reactive residues were deemed as extracellularly exposed in at least one DraNramp conformation; (2) NEM-reactive but MTSET-protected residues as intracellularly accessible; and (3) NEM-protected as buried (Figures S2C and S2D and Table S1). We observed high NEM accessibility all along TM1a and 6b, consistent with the large aqueous vestibule below the metal-binding residues in our structure. Between the metal-binding site and the extracellular face, we observed a helical pattern of accessible positions on TM1b, 3, and 6a that line the bundle-scaffold interface (Figure S2D). As many of these NEM-reactive positions are buried in the inward-facing structure (Figure 2A), we conclude that they face an aqueous pathway for periplasmic metal ions to reach the binding site in an alternate outward-open conformation. Thus, our cysteine accessibility measurements, rather than describing a single state, instead provide a composite picture of multiple conformations that DraNramp cycles through in the native membrane.

A Crystallization Construct Mutation Locks the Transporter in an Inward-Open State

We exploited this knowledge of the extracellular metal-permeation pathway to select A61C as a reporter to assess the conformational preferences of various DraNramp mutants (Figures 2A and 2B). A61C was accessible to inner membrane-impermeable modifier MTSET (Figure S2B), indicating that it faces a periplasmic aqueous environment, and A61C/C382S showed WT-level Co^{2+} transport (Figure S2E). In contrast, our crystallization construct, which contained entropy-reducing mutation patches in three intracellular loops: (1) QK169-70HH, (2) EEK251-3YYY, and (3) RR398-9HH, as well as an N-terminal 25-residue deletion (Figure S2F), did not transport Co^{2+} (Figure 2C). Patch 2 on its own completely eliminated Co^{2+} uptake (Figure 2C). This mutation is in intracellular loop 6–7, far from the metal-binding site; thus we tested A61C accessibility over a range of NEM concentrations to probe for conformational preference. Unlike the concentration-dependent increase in NEM modification of A61C for WT DraNramp, A61C was essentially not modified in the patch 2 background (Figures 2D and S2G). Therefore, the patch 2 mutant protein cannot switch to the outward-open state, which explains its loss-of-function phenotype, as substrate ions cannot reach the binding site (below A61C) from the outside. The patch 3 mutant had WT-level Co^{2+} transport and A61C modification, while the patch 1 mutant had

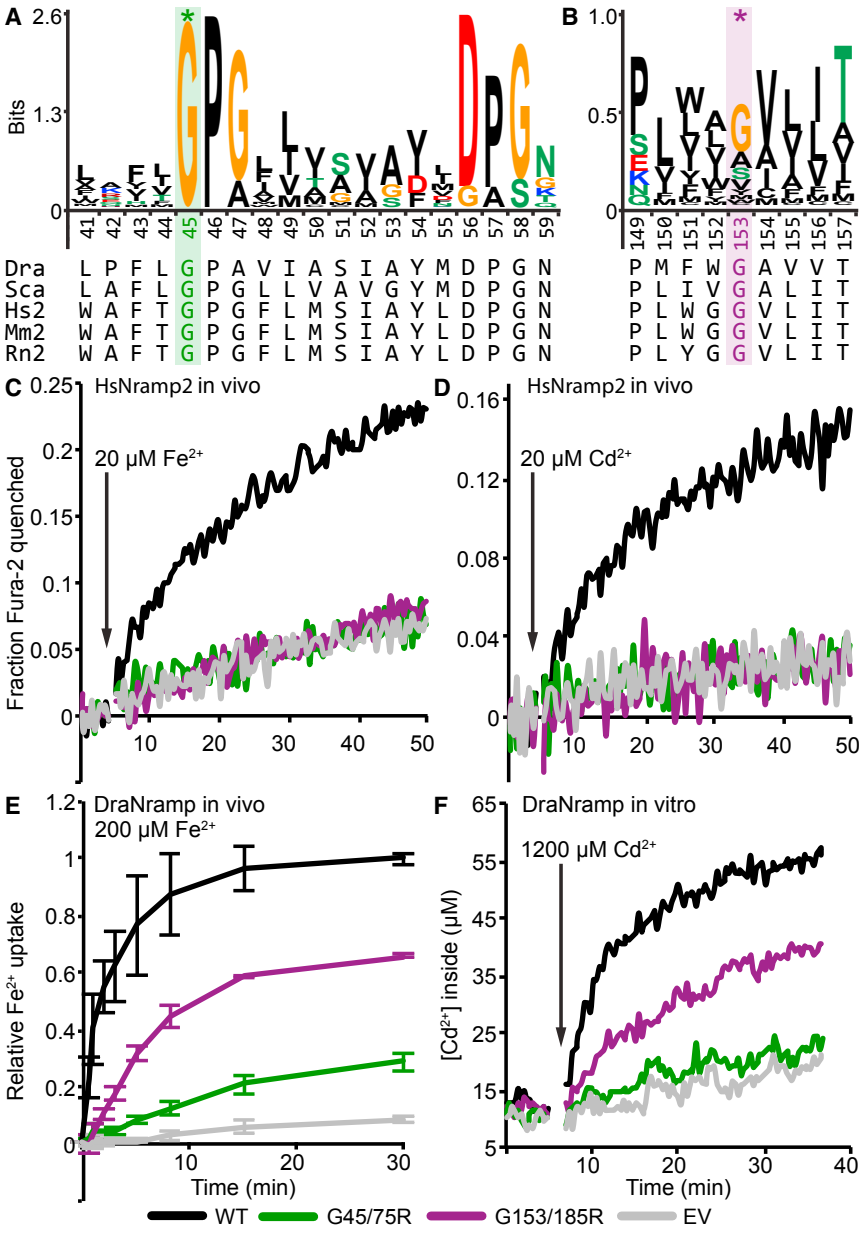

Figure 3. Glycine-to-Arginine Mutations Impair Transition Metal Transport in Both Human Nramp2 and DraNramp

(A and B) Sequence logos of the TM1a region (A) showing that G45 (shaded green with *, G75 in human Nramp2) on TM1a is absolutely conserved in Nramps, and a TM4 segment (B) showing that G153 (shaded purple with *, G185 in human/mouse/rat Nramp2) is generally a small amino acid. Logos were generated from an HMMER alignment of 2,691 sequences using DraNramp to search the UniProt database, with an E value cutoff of 1×10^{-9}. Dra, *D. radiodurans* MntH; Sca, *S. capitis* MntH; Hs2, *Homo sapiens* Nramp2; Mm2. *Mus musculus* Nramp2; and Rn2, *Rattus norvegicus* Nramp2.

(C and D) Fura-2 fluorescence quenching traces showing severe loss of function (no transport activity above baseline) for both G-to-R mutants compared with WT human Nramp2 for transport of the transition metals Fe^{2+} (C) and Cd^{2+} (D) in transfected HEK cells. Traces are representative of at least three independent transfection experiments.

(E) Relative Fe^{2+} uptake of *E. coli* expressing the analogous G-to-R DraNramp mutants also showed significantly decreased transport activity compared with WT. Plotted are averages ± SD (n = 3).

(F) Both G-to-R DraNramp mutants had decreased Cd^{2+} transport when reconstituted into proteoliposomes. Traces are representative of three experiments.

See also Figure S3.

both slightly reduced Co^{2+} transport and A61C accessibility (Figures 2C and 2D). This clear correlation of impaired metal uptake with loss of A61C accessibility further implicates the opening of the interface between the bundle and scaffold as an essential conformational change within the Nramp transport cycle.

Anemia-Causing Mutations Impair Metal Transport in Human Nramp2 and DraNramp

Naturally occurring glycine-to-arginine mutations G75R in TM1a in human Nramp2 and G185R in TM4 in mouse and rat Nramp2 all cause anemia (Blanco et al., 2009; Fleming et al., 1997, 1998). The TM1a glycine is absolutely conserved; the TM4 glycine is generally conserved as a small residue (Figures 3A and 3B). When introduced in human Nramp2, both G-to-R mutations abrogated transport of the physiological substrate Fe^{2+} (Figure 3C), as well as Cd^{2+}, Co^{2+}, and Mn^{2+} (Figures 3D, S3A, and S3B), as detected in transfected HEK cells using the metal-binding fluorescent dye Fura-2. Similarly, the analogous disease-mutant mimics in DraNramp significantly impaired Fe^{2+} transport as detected colorimetrically in DraNramp-expressing *Escherichia coli* (Figure 3E), and reduced Cd^{2+} (Figure 3F) and Mn^{2+} transport (Figure S3C) as detected with Fura-2 using purified DraNramp reconstituted into proteoliposomes. In both homologs, the TM1a G-to-R mutant expressed similarly to WT, while TM4 G-to-R mutant expression was reduced (Figures S3D and S3E), which could contribute to the loss-of-function phenotype in the in vivo assays. However, the DraNramp G153R mutation clearly impaired both Cd^{2+} and Mn^{2+} transport in proteoliposomes with normalized protein concentrations (Figure S3F). Notably, the G185R mutation in mouse Nramp2 similarly impaired Fe^{2+} transport (Su et al., 1998). These consistent loss-of-function data for the analogous mutants indicate that DraNramp is a useful model to further investigate how these disease-causing mutations inhibit transport.

The G153R Mutation Alters the Conformational Equilibrium and Metal Selectivity

G153 is far (~20 Å) from the metal-binding site, near the top of TM4 within the scaffold (Figure 4A). We tested the in vivo Co^{2+}

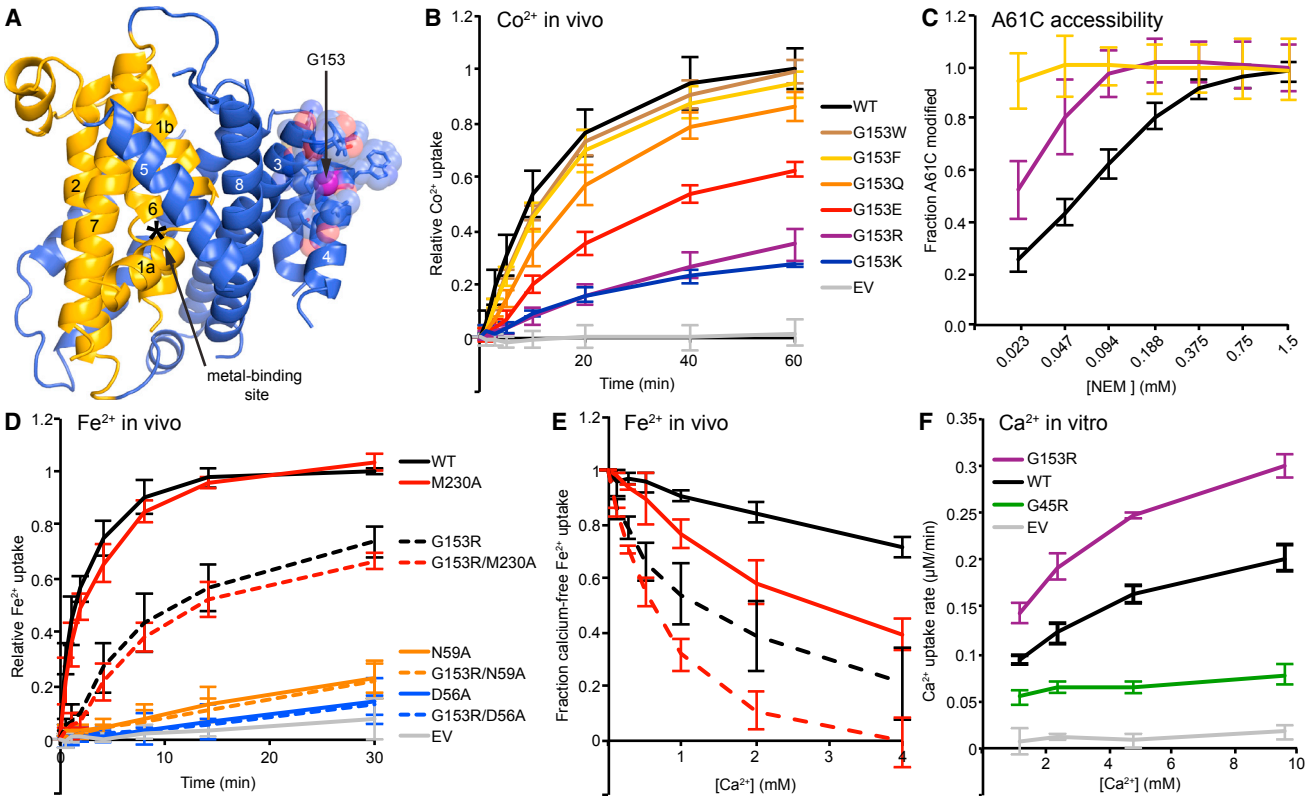

Figure 4. G153R Mutation Perturbs Outward-Facing State and Alters Metal Selectivity of the Binding Site to Favor Ca^{2+}

(A) In the inward-facing DraNramp structure, G153 is located on the extracellular end of TM4 tightly packed in the back of the scaffold, far from the conserved metal-binding site. The G153 Cα is a magenta sphere; nearby residues are shown as transparent spheres with side chains as sticks.

(B) Co^{2+} uptake data showing charged bulky substitutions at G153 reduced transport, while aromatic substitutions retained WT-level transport.

(C) G153R showed increased accessibility to NEM modification of the A61C outward-open conformational reporter, and G153F showed a further increase.

(D) In in vivo Fe^{2+} uptake, G153R showed little additional effect when combined with metal-binding site mutations, and its residual Fe^{2+} transport still uses the conserved metal-binding site as double mutations G153R/D56A and G153R/N59A both severely reduced transport.

(E) Competing Ca^{2+} reduced in vivo Fe^{2+} uptake more for G153R than WT, and double mutant G153R/M230A was even more susceptible to Ca^{2+} competition. The Ca^{2+}-free Fe^{2+} uptake level (2 min uptake for WT/M230A; 15 min uptake for G153 mutants) was set to 100% for each variant to facilitate direct % inhibition comparison.

(F) G153R transported more Ca^{2+} (as detected by Fura-2) than WT or the G45R mutant in an in vitro proteoliposome assay. All data are averages ± SD ($n \geq 3$). See also Figure S4.

uptake activity of various substitutions at this position. G153R, and the similarly large and positively charged G153K, were most impaired (Figure 4B). In contrast, replacing G153 with large aromatics (G153F and G153W) did not significantly alter Co^{2+} uptake (although Fe^{2+} uptake by G153F was somewhat reduced; Figure S4B). A negatively charged glutamate (G153E) reduced uptake much more than a polar glutamine (G153Q), although less than G153R. Overall, charged side chains caused the largest reductions in transport activity.

In our inward-open structure, modeling a bulky substitution at position 153 leads to major steric clashes with nearby residues such as I142 on TM3, indicating that G153R or similarly large substitutions likely alters DraNramp conformation at least locally. We therefore compared outward-open reporter A61C accessibility for this G153X panel (Figures 4C and S4C). All mutations resulted in increased NEM modification of A61C, with even more pronounced effects for G153F and G153W than for G153R. These data alone cannot distinguish between two scenarios: (1) increased occupancy of the outward-open state with concomitant decreased inward-open state occupancy; or (2) local structural changes that increase A61C accessibility in a protein that can still undergo conformational cycling. We further investigated this effect in Figure 6 (below).

Previous work showed that in mouse Nramp2 the G185R mutation decreased Fe^{2+} transport, but surprisingly enabled Ca^{2+} transport (Xu et al., 2004). This could occur through either distortion of the conserved metal-binding site or opening of an alternative metal-permeation pathway. We first tested whether the residual Fe^{2+} transport by G153R DraNramp relied on the canonical metal-binding site, introducing an alanine substitution for each binding-site side chain into the WT or G153R background. Either a D56A or N59A substitution abolished Fe^{2+} transport in both backgrounds, while M230A had negligible effects in both cases (Figure 4D), consistent with our previous results (Bozzi et al., 2016). Thus, G153R still relies on the conserved metal-binding residues for Fe^{2+} transport. We next tested whether

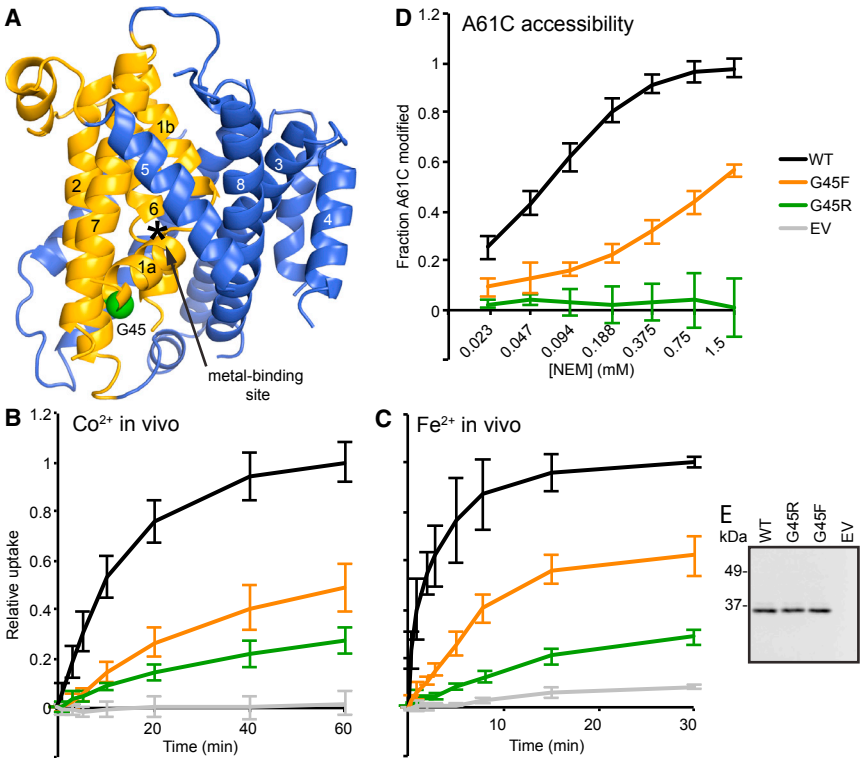

Figure 5. G45R Mutation Inhibits Transport by Locking Nramp in an Outward-Closed Conformation

(A) G45 (green sphere) is on TM1a on the intracellular side of the bundle, 11 residues below the metal-binding D56.

(B) G45R and G45F were significantly impaired in in vivo Co^{2+} transport.

(C) G45F also impaired in vivo Fe^{2+} transport (WT, G45R, and EV data reproduced from Figure 3E for comparison).

(D) G45R and G45F drastically decreased accessibility of outside-open conformational reporter A61C, indicating a strong preference for the inward-open state.

(E) Western blot showing G45R and G45F expressed similarly to WT DraNramp.

All data are averages ± SD ($n \geq 3$).

G153R perturbed the selectivity of this binding site by measuring Fe^{2+} transport in the presence of competing Ca^{2+} for WT, G153R, M230A, and G153R/M230A (Figure 4E), as well as G153F (Figure S4D). As expected, M230A, lacking the methionine "selectivity filter" that excludes alkaline earth metals (Bozzi et al., 2016), was more susceptible to Ca^{2+} competition than WT. Interestingly, G153R was even more susceptible to Ca^{2+}, and the G153R/M230A double mutant was most susceptible, as 4 mM Ca^{2+} effectively abolished Fe^{2+} uptake. This suggests that G153R indeed perturbs the metal-binding site in favor of Ca^{2+} in DraNramp in a manner that is complementary rather than redundant with removing the conserved methionine. We observed a similar pattern using a plate-based toxicity assay in which we assess the growth of *E. coli* expressing DraNramp or its variants on various metal concentrations: G153R or M230A increased Ca^{2+} susceptibility, and G153R/M230A again had an additive effect (Figure S4F). This synergy was not observed for the similar alkaline earth metal Mg^{2+}, as G153R/M230A had higher Mg^{2+} tolerance than M230A alone (Figure S4G), while G153R and WT grew similarly, suggesting that the G153R perturbation may be somewhat specific for Ca^{2+}. G153R also had a reduced susceptibility to Cd^{2+} compared with WT (Figure S4H), but was more susceptible than M230A. To directly demonstrate the improved Ca^{2+} transport of the G153R mutant, we purified and reconstituted it into proteoliposomes, and observed decreased Cd^{2+} transport (Figure S4E) but increased Ca^{2+} transport compared with WT (Figure 4F). Of note, the other disease-mutant mimic, G45R, impaired both Ca^{2+} and Cd^{2+} transport (Figure 4F), thus the metal specificity perturbation is unique to G153R. In summary, the G153R mutation in our bacterial DraNramp model system alters the conserved metal-binding site in a manner that both improves Ca^{2+} transport and impairs transition metal transport, analogously to mouse Nramp2.

The G45R Mutation Wedges the Transporter in an Inward-Facing Conformation

Like G153, the completely conserved G45 is ~20 Å away from the metal-binding site at the N terminus of TM1a, which juts out at an angle to provide high cytoplasmic solvent access to the metal-binding residues (Figure 5A). Modeling an arginine at this position in our inward-facing structure yields no steric clash. We thus hypothesized that the mutation is not tolerated in the alternate outward-open state: a bulky residue at this position may act as a wedge forcing the protein to remain in the inward-open state, thus explaining the severe metal-transport impairment of G45R (Figure 3). Consistently, the bulky uncharged G45F substitution impaired in vivo uptake of Co^{2+} (Figure 5B) and Fe^{2+} (Figure 5C) nearly as much as G45R. Furthermore, single-cysteine reporter A61C was essentially fully protected in G45R, indicating that the outward-open state was rarely if ever sampled, while A61C accessibility in G45F suggested a shifted conformational preference, strongly favoring the inward-open state relative to WT (Figure 5D). Thus, decreased A61C accessibility of G45 substitutions correlated with decreased metal transport. This is similar to the patch mutant phenotypes (Figures 2C and 2D), especially patch 2, which just like G45 is located in the intracellular half of the bundle, indicating the importance of proper conformational cycling for protein function.

Mutations at Glycine Positions Illustrate the Conformational Change Process in DraNramp

To further explore the DraNramp conformational cycle, we investigated how G45R and G153F altered solvent accessibility for a panel of inward- or outward-accessible single-cysteine substitutions that retained significant transport activity (Figures S5A and S5B). Accessibility of outward reporters A61C and L140C was correlated; G45R greatly decreased while G153F greatly

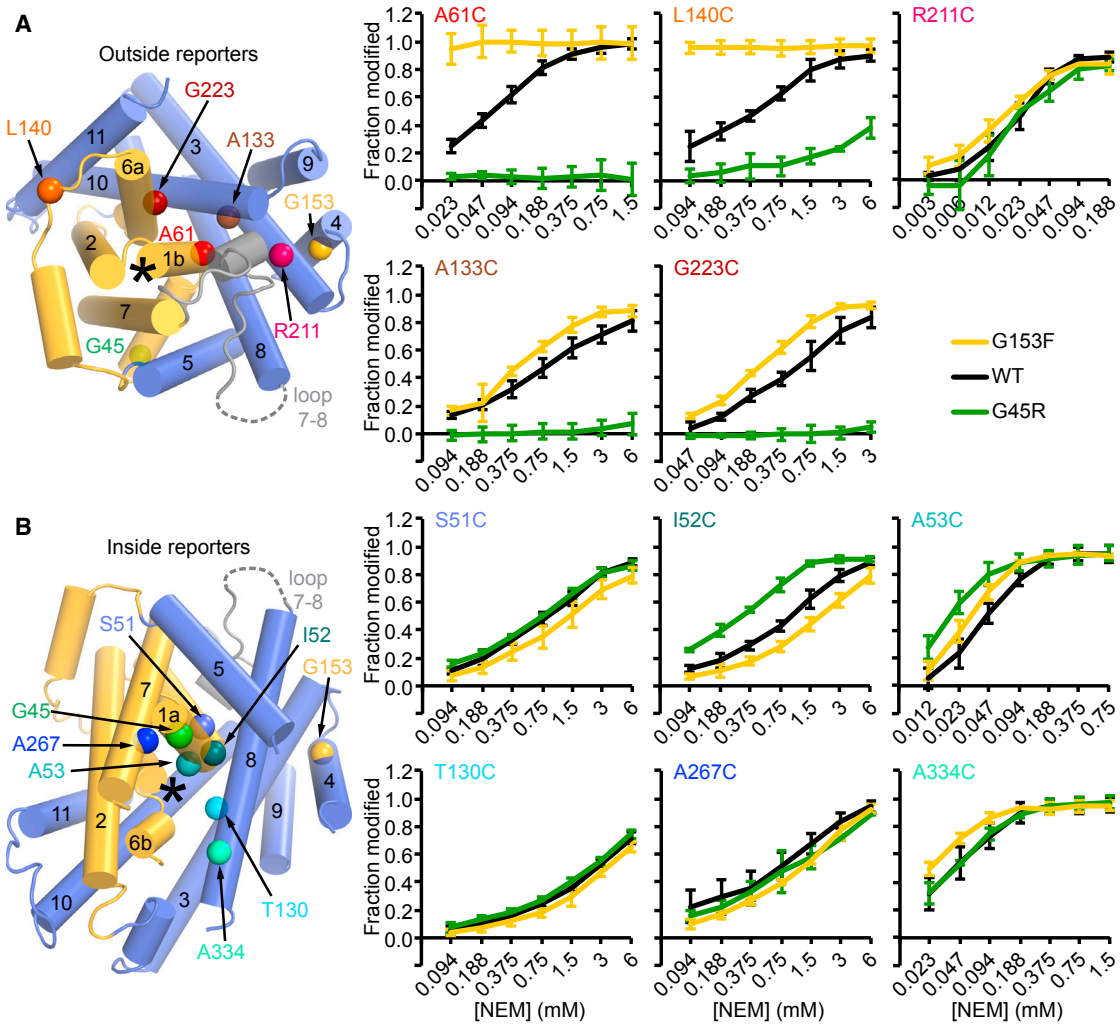

Figure 6. Mutations of Conserved Glycines Shift the Conformational Landscape of DraNramp

(A) Cysteine modification as a function of NEM concentration for five extracellularly accessible reporters, mapped on a top view of the structure (left). A61C data are repeated from Figures 3C and 4D for comparison.

(B) NEM modification for five intracellularly accessible cysteine reporters, as well as T130C, which could not clearly be assigned as intracellularly or extracellularly accessible. Reporter positions are indicated on the structure, viewed down the cytoplasmic vestibule.

* indicates the metal-binding site. All data are averages ± SD ($n \geq 4$). See also Figure S5.

increased accessibility (Figure 6A). This suggests that G153F favors a conformational state in which part of the bundle-scaffold interface above the metal-binding site is highly exposed (perhaps by dislodging loop 7–8 that blocks solvent access to A61 and L140 in the inward-open structure). Closer to the metal-binding site within the bundle-scaffold interface, outward-accessible G223C and A133C were also fully protected in G45R, further supporting our inward-locked model for G45R (Figure 6A). However, at those cysteine positions G153F only had a modest effect, slightly increasing accessibility. Finally, neither G45R nor G153F altered accessibility of R211C on extracellular loop 5–6.

Accessibility was also unaltered at T130C, on TM3 adjacent to the unwound regions of TM1 and 6, indicating that the metal-binding site remains solvent-accessible in both G153F and G45R (Figure 6B).

To probe for water-excluding structural changes in the cytoplasmic vestibule, we compared NEM accessibility of five cysteines located below the metal-binding site in the WT, G45R, and G153F backgrounds (Figure 6B). Accessibility was the same in all backgrounds for S51C on TM1a, A267C on TM7, and A334C on TM8. For I52C and A53C on TM1a just below the metal-binding D56, accessibility was higher in G45R, suggesting that these positions form part of the cytoplasmic gate regulating access to the metal-binding site. We observed only minor perturbations at all inward-reporter positions for G153F. Thus, this mutation likely does not lock the protein in the outward-facing state with a closed intracellular gate, consistent with its high metal-transport activity (Figures 4B and S4B). In summary, the intracellular gate likely includes the TM1a C terminus, although a more complete picture awaits a truly outward-locked mutant. On the extracellular side, our crystal structure

and cysteine accessibility results clearly demonstrate a ~15 Å thick, solvent-excluding gate that remains firmly closed in the G45R mutant.

TM1a Movement Is Essential to the DraNramp Transport Cycle

To determine the functional importance of the DraNramp N terminus, we designed a truncation series that eliminated 25–49 residues (Figures S6A–S6C). Co^{2+} uptake activity was at WT levels up through the ΔN34 construct, and slight reductions in transport accompanied each further truncation for ΔN37, ΔN40, and ΔN43 (Figure S6). In contrast, ΔN46 and ΔN49, which both truncate beyond the TM1a N terminus at the invariant G45, showed pronounced drops in Co^{2+} uptake activity.

To further assess the importance of TM1a movement for metal transport, we compared Co^{2+} uptake for single-cysteine mutants, either unmodified or pre-modified with NEM (Figure 7A). For cysteine-less mutant C382S, WT (with the inaccessible C382), and extracellular loop control R211C, NEM treatment did not impair transport. However, for six of seven TM1a positions where the cysteine mutant retained transport activity, NEM modification greatly impaired transport. Thus, while those cysteines were highly accessible in at least one conformation, they must move into a more congested environment as part of the metal-transport cycle, which NEM modification sterically blocks. This phenomenon was not observed for positions preceding TM1a (residues 40–44, disordered in the structure). Cysteine substitution alone impaired transport at four positions: G45C, consistent with the importance of this conserved glycine and loss of function of G45R and G45F (Figures 3 and 5); D56C and G58C, which disrupt the metal-binding site; and A50C, a surprising result given the subtle size increase, which may reflect how close this face of TM1a must approach TM7 and/or the scaffold (TM8) as the inside gate closes in the outward-open state. Surprisingly, we did not observe NEM-dependent impairment for the two accessible TM1b positions A61C and E65C, the first of which clearly lines the outward metal-permeation pathway and is buried in the inward-open state. An A61W mutant similarly retained WT-level Co^{2+} transport, showing that DraNramp can indeed tolerate added bulk at this position (Figure S6D). However, pre-modifying A61C with the positively charged MTSET selectively inhibited Co^{2+} uptake (Figure S6G), thus some perturbation of the outward metal-permeation pathway at position A61 can indeed disrupt transport.

Finally, to further test the functional importance of TM1a movement, we substituted tryptophan (an alternative way of adding steric bulk) at each of the six TM1a positions where NEM modification of cysteine mutants drastically impaired transport. Analogously to G45R, these tryptophan mutations greatly impaired Co^{2+} transport and fully protected the A61C outward-open reporter (Figures S6D–S6F), indicating that bulky modifications on TM1a lock the protein in an inward-facing conformation. In summary, these results indicate that TM1a movement is an integral part of Nramp conformational rearrangement and is thus required for metal transport. From all of our results, we propose a model of Nramp conformational change in which significant inward movement of TM1a toward the scaffold is crucial to opening the outside interface between the bundle (TM1b and 6a) and scaffold (TM3, 8, and 10) to allow metal ions (and bulk water) to access the binding site from the outside (Figure 7B).

DISCUSSION

Using X-ray crystallography, cysteine accessibility, and metal-transport measurements, we developed DraNramp as a model to understand the conformational change process for the Nramp family of divalent metal transporters. The DraNramp structure, while also a LeuT fold in an inward-facing conformation, complements the ScaNramp structure (Ehrnstorfer et al., 2014) by identifying the location of the functionally important TM1a and (with cysteine-scanning mutagenesis) the external metal-permeation pathway. It also provides a structural example of a second distinct evolutionary clade within the Nramp family. Furthermore, our structure showed the locations of two highly conserved glycines where mutations to arginine cause anemia in either rodents (Fleming et al., 1997, 1998) or humans (Blanco et al., 2009) and impair transport in both human Nramp2 and DraNramp (Figure 3).

The G153R mutation on DraNramp TM4 mimics the phenotype first observed in mouse Nramp2 (Xu et al., 2004), altering metal-transport selectivity, despite these two homologs having only 29% sequence identity. G153R perturbs the conserved metal-binding site, thus reducing transport of the typical transition metal substrates of Nramp and increasing Ca^{2+} transport (Figure 4). A bulky residue cannot be accommodated at position 153 in our inward-facing structure. Our data are consistent with the G153R mutation distorting the scaffold in a manner that interferes with closing of the extracellular metal-permeation pathway (Figure 6). Precisely how a mutation 20 Å from the binding site increases Ca^{2+} permeability remains undetermined, but interestingly G153R and M230A, which remove the sulfur ligand responsible for excluding alkaline earth metals (Bozzi et al., 2016), have additive effects (Figures 4 and S4). Other residues besides the four previously identified may be important to metal binding and/or selectivity and, in at least one other Nramp homolog, mutations distant from the metal-binding site affect substrate preference (Pottier et al., 2015).

G45R on TM1a forms a steric wedge that prevents the protein from reaching the outward-open state (Figure 5). Moreover, our results imply that the unfettered movement of TM1a is essential to the conformational rearrangement that must occur to allow metal transport (Figures 7 and S6).

Our study adds to a wealth of structural and functional information available for LeuT-fold secondary transporters (Penmatsa and Gouaux, 2014; Shi, 2013) that expanded on the original "rocking bundle" model of alternating access in which the bundle (TM1, 2, 6, and 7) moves relative to the scaffold (Forrest and Rudnick, 2009; Forrest et al., 2008). Comparison of outward- and inward-open LeuT structures (Krishnamurthy and Gouaux, 2012) showed TM1a swinging up by 45° and a smaller TM6b motion exposing the substrate-binding site to the cytosol. However, the physiological relevance of this large TM1a movement in LeuT is disputed: while some movement is essential to substrate release (Zhao et al., 2011), the Y268A mutation on TM6b in the crystallized construct disrupts a hydrogen-bonding network in the inward-facing state and stabilizes a conformation not highly sampled by the WT protein (Kazmier et al., 2014b),

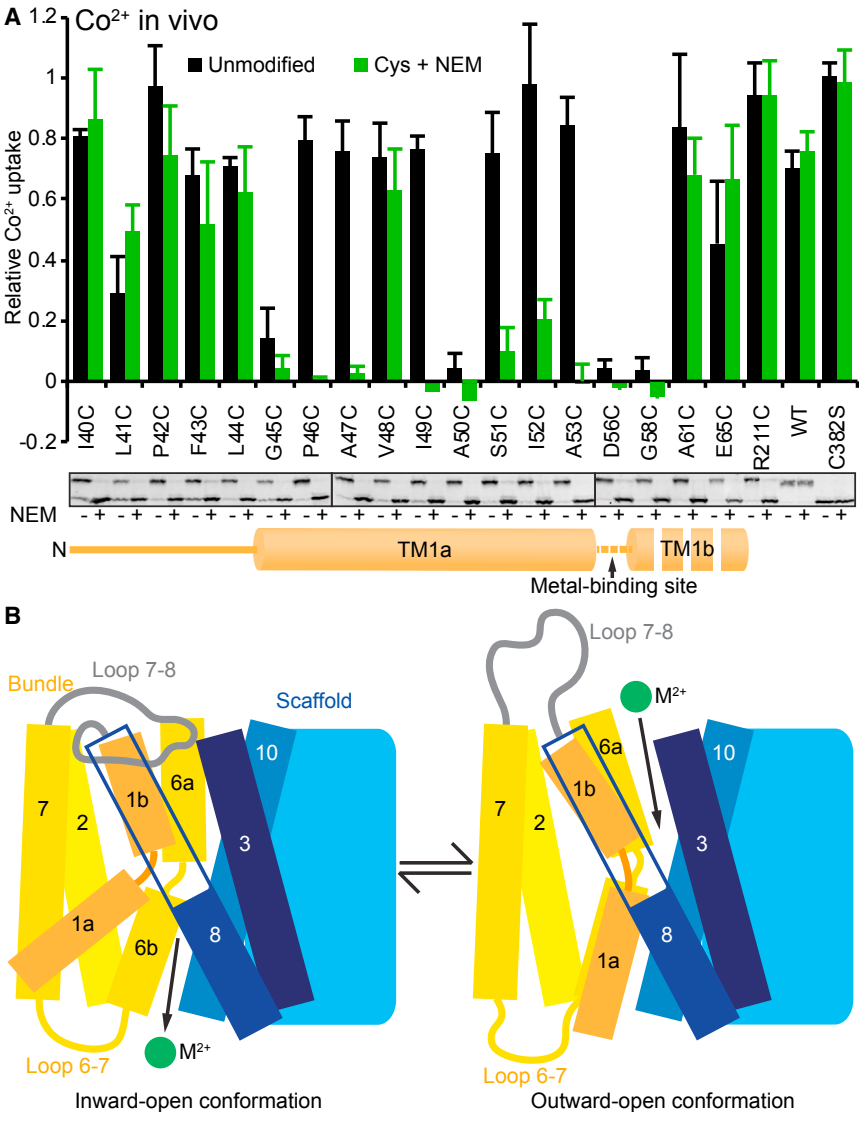

Figure 7. TM1a Movement Is Essential to the Conformational Change that Opens the Outward Metal-Permeation Pathway, thus Enabling Nramp Metal Transport

(A) Initial (6 min) in vivo Co^{2+} transport (minus EV control) for accessible single-cysteine mutants along TM1 that were either left unmodified (black bars) or pre-reacted with NEM (3 mM; green bars). NEM modification greatly impaired transport for six out of the seven TM1a positions where cysteine mutants had high transport activity. Data are averages ± SD (n = 3). Western blots show that all introduced cysteines were efficiently NEM labeled, as preincubation with NEM (+) prevented formation of 5 kDa PEG maleimide DraNramp (upper band in the [−] lanes). R211C on extracellular loop 5–6 was readily NEM modified without affecting activity. Endogenous C382 on TM10 in WT was not modified by NEM, and thus was fully modified by 5 kDa PEG maleimide. The cysteine-less C382S is not labeled by either NEM or 5 kDa PEG maleimide.

(B) Model of the conformational change process in DraNramp. Our metal transport and cysteine accessibility results demonstrated that the unencumbered TM1a movement is essential for conformational change into the outward-facing state, including evicting loop 7–8 which caps the outside metal-permeation pathway and opening the interface between the bundle (TM1b and 6a) and scaffold (TM3, 8, and 10), thus allowing periplasmic metal ions to reach the binding site in the unwound regions of TM1 and 6 at the center of the membrane plane. See also Figure S6.

with molecular dynamics simulations also supporting a less-drastic tilt in a lipid bilayer environment (Grouleff et al., 2015). In DraNramp, our inward-locking patch 2 mutant and/or crystal-packing interactions with the Fab could analogously stabilize the observed profound TM1a kink. Additional Nramp structures will help to clarify this issue.

We nevertheless predict that TM1a undergoes significant displacement during the conformational change process, given its functional importance in DraNramp. In addition, the LeuT structures showed that movement of TM1b and 6a away from the scaffold opens an aqueous pathway to the binding site, in agreement with our DraNramp cysteine accessibility data. Furthermore, these LeuT structures and functional studies (Claxton et al., 2010) illustrated the contribution of loop 7–8 to closing off extracellular access to the substrate-binding site, which we also observe in DraNramp.

Structural information on other sodium-coupled symporters of small organic molecules hints at the mechanistic diversity within the LeuT-fold family. Structures of the sodium/galactose transporter vSGLT show a TM1a movement (subtler than in LeuT) to open the inside gate in the transition from the inward-occluded to the inward-open state (Watanabe et al., 2010). In the sodium/betaine transporter BetP, outward- and inward-open structures also show TM1a motion as part of the inside gate, whereas loop 7–8 is similarly positioned above the bundle-scaffold interface but does not appear to move much (Perez et al., 2012). Crystallographic (Shimamura et al., 2010) and electron paramagnetic resonance (Kazmier et al., 2014a) studies of the sodium/nucleobase symporter Mhp1 showed a mechanism similar to LeuT albeit with subtle differences: TM5 rather than TM1a bends to open the inner gate and TM10 (and to a lesser extent loop 7–8) changes conformation to close the outer gate.

Our combined structural and functional results thus suggest that the conformational change process of Nramp may be most similar to that of LeuT. However, the proposed proton co-substrate(s) of Nramp would require a unique transport mechanism and lead to different environmental controls of its conformational landscape, perhaps with a protonation event substituting for the Na^+ coordination that governs LeuT conformational preference (Malinauskaite et al., 2014; Tavoulari et al., 2016). Ultimately, a complementary outward-open Nramp crystal structure will help answer outstanding questions regarding the Nramp transport cycle.

EXPERIMENTAL PROCEDURES

Cloning of Nramp Constructs

The DraNramp sequence was inserted into the NdeI and NotI sites of pET21-N8H and human Nramp2 into pCDNA3 vectors as described previously (Bozzi et al., 2016). Mutagenesis was performed using QuikChange protocols (Stratagene), and confirmed by sequencing.

DraNramp Protein Purification

DraNramp C41(DE3) cells were grown at 37°C in 12 L of terrific broth with 10% (w/v) glycerol and 100 mg/L ampicillin, inoculating with 1:50 overnight culture to an optical density at 600 nm of 1.0, induced with 100 μM isopropyl-β-D- thiogalactoside for 4 hr. Proteins were purified at 4°C. Cells were lysed by sonication in three volumes of lysis buffer (20 mM $NaPO_4$ [pH 7.0], 75 mM imidazole-HCl [pH 7.0], 500 mM NaCl, 10% glycerol) plus 1 mM PMSF, 1 mM benzamidine, 0.3 mg/mL each DNAse I and lysozyme. Debris was removed by 20 min centrifugation at 27,000 × *g*, membranes were pelleted in 70 min at 230,000 × *g*, solubilized in 35 mL lysis buffer +1% (w/v) β-dodecylmaltoside (DDM) for 1 hr, and clarified by 35 min centrifugation at 140,000 × *g*, filtered through a 0.45 μm filter, loaded onto 5 mL Ni-Sepharose (GE Healthcare) pre-equilibrated with lysis buffer + 0.03% β-DDM, and washed thrice with 50 mL lysis +0.03% β-DDM. Protein was eluted in 25 mL increasing imidazole to 450 mM, and concentrated to ~1 mL in a 50 kDa cutoff centrifugal concentrator. Following buffer exchange on a Superdex S200 (GE Healthcare) to 20 mM HEPES (pH 7.5), 150 mM NaCl, and 0.1% (w/v) β-decylmaltoside (DM), protein-containing fractions were identified using SDS-PAGE, pooled, and concentrated to ~5 mg/mL.

Fab Production

BALB/c mice were immunized four times with DraNramp reconstituted into proteoliposomes using *E. coli* lipids (Avanti Polar Lipids). All procedures were approved by the Massachusetts Institute of Technology Committee on Animal Care. Hybridomas were generated and cultured using established protocols (Yokoyama, 2008), and secreted monoclonal antibodies (mAbs) were tested in ELISA by being captured on anti-mouse IgG-coated 96-well plates. Binding mAbs were identified using detergent-solubilized biotinylated DraNramp coupled to streptavidin-horseradish peroxidase. Cells in ELISA-positive wells underwent four rounds of recloning by limiting dilution to ensure monoclonality and stable mAb expression. Conformation-specific mAb clones were selected as non-binders in slot blot assays for binding to SDS-denatured DraNramp. The cocrystallized mAb was purified by capture from filtered hybridoma supernatant on protein A-agarose pre-equilibrated with binding buffer (BB; 20 mM $NaPO_4$ [pH 8.0], 150 mM NaCl). After a ten-column-volume BB wash, mAbs were eluted in seven column volumes of 100 mM 2-(N-morpholino)ethanesulfonic acid (pH 6.5) and 3.6 M $MgCl_2$, dialyzed against BB, and concentrated using a 50 kDa cutoff concentrator. Purified mAbs (15 mg at 1.5 mg/mL) in 20 mM $NaPO_4$, 20 mM EDTA (pH 6.0) were digested with 5 units of ficin suspension (Sigma-Aldrich) at room temperature for 5 hr. After adding 50 mg iodacetamide and 50 mg N-ethyl maleimide, the digest was concentrated and run on a Superdex S200 16/600 (GE Healthcare) in BB. Fab-containing fractions were passed through 5 mL protein A-agarose to remove any Fc fragment or uncleaved mAb, and concentrated to ~10 mg/mL. The Fab sequence was obtained using standard protocols (Verma, 2000).

Fab Crystallization and Structure Determination

Fab crystals were grown by sitting drop-vapor diffusion, mixing 0.5 μL 10 mg/mL Fab with 0.5 μL reservoir (0.1 M 3-(cyclohexylamino)-1-propanesulfonic acid [pH 9.7], 0.1 M $MgCl_2$, 30% polyethylene glycol [PEG] 3350), cryoprotected in the reservoir plus 25% glycerol, and frozen in liquid nitrogen. Diffraction data to 3.1 Å were collected at the Advanced Photon Source beamline ID24-E (Table 1). An Igg2b Fab structure (PDB: 1KNO) was used as a MR search model, and the Fab structure was refined to R_{work}/R_{free} of 0.22/0.30 using REFMAC.

DraNramp-Fab Crystallization and Structure Determination

The DraNramp crystallization construct was truncated by 25 residues at the N terminus, and mutations were introduced in intracellular loops (QK169-170HH, EEK251-3YYY, and RR398-9HH). DraNramp was incubated for 2 hr with Fab in a 1:1.2 molar ratio, and run on a Superdex S200 10/300 (GE Healthcare) in 10 mM HEPES (pH 7.5), 150 mM NaCl, and 0.1% DM. DraNramp-Fab-containing fractions were pooled and concentrated to ~5–10 mg/mL using a 50 or 100 kDa cutoff concentrator. DraNramp-Fab crystals were grown by vapor diffusion against 0.1 M sodium acetate (pH 4.5), 0.05 M magnesium acetate, 24% PEG 400, and 0.4%–1% β-octylglucoside in 1:1 volume ratio of sitting drops at 4°C. Crystals derivatized with 1 mM $OsCl_3$ for 1 day turned dark brown and were frozen in liquid nitrogen.

Diffraction data were collected from three crystals at the Advanced Photon Source ID24-E and -C beamlines, using vector scanning and full transmission, processed with HKL2000 (Otwinowski and Minor, 1997), and merged to improve completeness. For initial phasing, a ScaNramp-based homology DraNramp model built using SWISS MODEL (Biasini et al., 2014) and the Fab structure were used as MR search models in Phaser (McCoy et al., 2007). Experimental phase information from single-wavelength anomalous diffraction from the osmium-soaked crystals was determined using AutoSol in PHENIX (Adams et al., 2010). The resulting osmium sites were combined with the MR solution and data containing the experimental phase information were used for refinement. Coot (Emsley and Cowtan, 2004) was used for model building. Initial rounds of refinement used xMDFF, with input files prepared in VMD (Humphrey et al., 1996) using the MDFF-GUI (McGreevy et al., 2016) with default molecular dynamics parameters (McGreevy et al., 2014), improving R_{work}/R_{free} from 0.50/0.54 to 0.41/0.45. The model was further refined using PHENIX with additional local refinements using xMDFF. TM1a was placed using a combination of xMDFF and steered molecular dynamics (SMD) simulations. As with the CiVSP voltage sensor protein (Li et al., 2014), a helix-screw motion was induced in SMD simulations using the orientation quaternion (Jiang et al., 2014) of the helix as a collective variable, while simultaneously using electron density restraints. The TM1a helix position featuring the lowest R value was identified, resulting in a 2% increase in the local cross-correlation. It is also consistent with cysteine accessibility data (Figure 6). After final rounds of refinement in PHENIX, the final model includes residues 43–165, 176–236, 259–304, 310–341, 353–428 for DraNramp, 1–129 + 132–213 and 1–213 for the Fab heavy and light chains, respectively, and three osmium ions. Figures were made in PyMOL (Schrödinger).

Cysteine Accessibility Measurements

Adapting the cysteine-labeling protocol from Tetsch et al., (2011), *E. coli* expressing single-cysteine DraNramp variants were exposed to thiol modifiers in 100 mM Tris (pH 7), 60 mM NaCl, 10 mM KCl, 0.5 mM $MgCl_2$, and 0.75 mM $CaCl_2$. All incubations were at 37°C. To determine overall accessibility, 3 mM NEM was applied for 60 min. To determine inside versus outside accessibility, 3 mM MTSEA or MTSET was applied for 30 min followed by 1.5 mM NEM for 30 min. For all NEM-gradient experiments, the indicated NEM concentration was applied for 15 min at room temperature. Excess cysteine was added to quench reactions. Cells were washed twice, resuspended and incubated 1 hr in 100 mM Tris (pH 7), 6 M urea, 0.5% SDS, and 0.5 mM DTT, incubated with a 2-fold excess of 5 kDa PEG maleimide (Creative PEGWorks), then quenched with sample buffer containing β-mercaptoethanol. Protein was detected in western blots using an Alexa 647-conjugated anti-His-tag antibody (QIAGEN) and a Typhoon Imager (GE Healthcare), and background-subtracted band intensities (I) were measured using ImageJ64. The upper (5-kDa PEG maleimide modified) to lower band (NEM modified) ratio was determined and compared with the no-NEM sample ratio (defined as maximal upper-to-lower band ratio = 0% NEM modified) to calculate the NEM-modified cysteine fraction using: modified-cysteine fraction = $1 - [I_{upper}/(I_{lower} + I_{upper})]/[I_{upper\text{-}no\text{-}NEM}/(I_{lower\text{-}no\ NEM} + I_{upper\text{-}no\text{-}NEM})]$.

Metal Uptake Assays

Metal-transport experiments in proteoliposomes, *E. coli*, and HEK293T cells were performed as described previously (Bozzi et al., 2016). See the Supplemental Information for additional description.

ACCESSION NUMBERS

The accession number for the DraNramp crystal structure reported in this paper is PDB: 5KTE. The unprocessed diffraction images used to determine the Fab and DraNramp structures were deposited in the Structural Biology Data

Grid (https://data.sbgrid.org/) with accession numbers SBDG: 332, 333, 334, 335.

SUPPLEMENTAL INFORMATION

Supplemental Information includes Supplemental Experimental Procedures, six figures, and one table and can be found with this article online at http://dx.doi.org/10.1016/j.str.2016.09.017.

AUTHOR CONTRIBUTIONS

R.G. oversaw and designed the research with W.A.W., L.B.B., and A.T.B.; W.A.W. and E.R.G. generated mAbs, which H.L.P. supervised; W.A.W. obtained DraNramp-Fab crystals and all diffraction data; L.B.B. purified DraNramp mutants and determined the DraNramp-Fab structure; L.B.B. and A.T.B. developed in vitro metal-transport assays; A.T.B. made most Nramp mutants, performed all cysteine accessibility and metal-transport experiments, and analyzed the resulting data; A.S. performed the xMDFF and SMD simulations, which K.S. supervised; A.T.B., L.B.B., and R.G. wrote the manuscript, with input from all authors.

ACKNOWLEDGMENTS

We thank Alexandra Rojek for selecting and cloning several single-cysteine DraNramp mutants, Brandon Lee for help with developing the NEM pre-modification cobalt uptake assay, Jack Nicoludis, Christina Zimanyi, and members of the Gaudet Lab for discussions. The work was funded in part by a Basil O'Connor Starter Scholar Research Award from the March of Dimes Foundation (to R.G.), grant NIH 9P41GM104601 (to K.S.), and a Beckman Postdoctoral Fellowship (to A.S.). We gladly acknowledge supercomputer time from the Texas Advanced Computing Center via Extreme Science and Engineering Discovery Environment grant NSF-MCA93S028. We thank the NE-CAT beamline staff at the Advanced Photon Source (Argonne, IL, USA) for help with data collection. NE-CAT is funded by NIH (P41 GM103403 and S10 RR029205), and the Advanced Photon Source by the U.S. Department of Energy (DE-AC02-06CH11357).

Received: July 13, 2016
Revised: September 27, 2016
Accepted: October 7, 2016
Published: November 10, 2016

REFERENCES

Abbaspour, N., Hurrell, R., and Kelishadi, R. (2014). Review on iron and its importance for human health. J. Res. Med. Sci. *19*, 164–174.

Adams, P.D., Afonine, P.V., Bunkoczi, G., Chen, V.B., Davis, I.W., Echols, N., Headd, J.J., Hung, L.W., Kapral, G.J., Grosse-Kunstleve, R.W., et al. (2010). PHENIX: a comprehensive Python-based system for macromolecular structure solution. Acta Crystallogr. D Biol. Crystallogr. *66*, 213–221.

Aisen, P., Enns, C., and Wessling-Resnick, M. (2001). Chemistry and biology of eukaryotic iron metabolism. Int. J. Biochem. Cell Biol. *33*, 940–959.

Andrews, N.C. (2008). Forging a field: the golden age of iron biology. Blood *112*, 219–230.

Barrios, M., Moreno-Carralero, M.I., Cuadrado-Grande, N., Baro, M., Vivanco, J.L., and Moran-Jimenez, M.J. (2012). The homozygous mutation G75R in the human SLC11A2 gene leads to microcytic anaemia and iron overload. Br. J. Haematol. *157*, 514–516.

Biasini, M., Bienert, S., Waterhouse, A., Arnold, K., Studer, G., Schmidt, T., Kiefer, F., Gallo Cassarino, T., Bertoni, M., Bordoli, L., et al. (2014). SWISS-MODEL: modelling protein tertiary and quaternary structure using evolutionary information. Nucleic Acids Res. *42*, W252–W258.

Blanco, E., Kannengiesser, C., Grandchamp, B., Tasso, M., and Beaumont, C. (2009). Not all DMT1 mutations lead to iron overload. Blood Cells Mol. Dis. *43*, 199–201.

Bozzi, A.T., Bane, L.B., Weihofen, W.A., McCabe, A.L., Singharoy, A., Chipot, C.J., Schulten, K., and Gaudet, R. (2016). Conserved methionine dictates substrate preference in Nramp-family divalent metal transporters. Proc. Natl. Acad. Sci. USA *113*, 10310–10315.

Canonne-Hergaux, F., Fleming, M.D., Levy, J.E., Gauthier, S., Ralph, T., Picard, V., Andrews, N.C., and Gros, P. (2000). The Nramp2/DMT1 iron transporter is induced in the duodenum of microcytic anemia mk mice but is not properly targeted to the intestinal brush border. Blood *96*, 3964–3970.

Canonne-Hergaux, F., Zhang, A.S., Ponka, P., and Gros, P. (2001). Characterization of the iron transporter DMT1 (NRAMP2/DCT1) in red blood cells of normal and anemic mk/mk mice. Blood *98*, 3823–3830.

Cellier, M.F. (2012). Nramp: from sequence to structure and mechanism of divalent metal import. Curr. Top Membr. *69*, 249–293.

Cellier, M.F., Bergevin, I., Boyer, E., and Richer, E. (2001). Polyphyletic origins of bacterial Nramp transporters. Trends Genet. *17*, 365–370.

Cellier, M.F., Courville, P., and Campion, C. (2007). Nramp1 phagocyte intracellular metal withdrawal defense. Microbes Infect. *9*, 1662–1670.

Claxton, D.P., Quick, M., Shi, L., de Carvalho, F.D., Weinstein, H., Javitch, J.A., and McHaourab, H.S. (2010). Ion/substrate-dependent conformational dynamics of a bacterial homolog of neurotransmitter:sodium symporters. Nat. Struct. Mol. Biol. *17*, 822–829.

Courville, P., Chaloupka, R., and Cellier, M.F. (2006). Recent progress in structure-function analyses of Nramp proton-dependent metal-ion transporters. Biochem. Cell Biol. *84*, 960–978.

Ehrnstorfer, I.A., Geertsma, E.R., Pardon, E., Steyaert, J., and Dutzler, R. (2014). Crystal structure of a SLC11 (NRAMP) transporter reveals the basis for transition-metal ion transport. Nat. Struct. Mol. Biol. *21*, 990–996.

Emsley, P., and Cowtan, K. (2004). Coot: model-building tools for molecular graphics. Acta Crystallogr. D Biol. Crystallogr. *60*, 2126–2132.

Fleming, M.D., Trenor, C.C., 3rd, Su, M.A., Foernzler, D., Beier, D.R., Dietrich, W.F., and Andrews, N.C. (1997). Microcytic anaemia mice have a mutation in Nramp2, a candidate iron transporter gene. Nat. Genet. *16*, 383–386.

Fleming, M.D., Romano, M.A., Su, M.A., Garrick, L.M., Garrick, M.D., and Andrews, N.C. (1998). Nramp2 is mutated in the anemic Belgrade (b) rat: evidence of a role for Nramp2 in endosomal iron transport. Proc. Natl. Acad. Sci. USA *95*, 1148–1153.

Forrest, L.R., and Rudnick, G. (2009). The rocking bundle: a mechanism for ion-coupled solute flux by symmetrical transporters. Physiology (Bethesda) *24*, 377–386.

Forrest, L.R., Zhang, Y.W., Jacobs, M.T., Gesmonde, J., Xie, L., Honig, B.H., and Rudnick, G. (2008). Mechanism for alternating access in neurotransmitter transporters. Proc. Natl. Acad. Sci. USA *105*, 10338–10343.

Ganz, T. (2009). Iron in innate immunity: starve the invaders. Curr. Opin. Immunol. *21*, 63–67.

Grouleff, J., Sondergaard, S., Koldso, H., and Schiott, B. (2015). Properties of an inward-facing state of LeuT: conformational stability and substrate release. Biophys. J. *108*, 1390–1399.

Gunshin, H., Mackenzie, B., Berger, U.V., Gunshin, Y., Romero, M.F., Boron, W.F., Nussberger, S., Gollan, J.L., and Hediger, M.A. (1997). Cloning and characterization of a mammalian proton-coupled metal-ion transporter. Nature *388*, 482–488.

Gunshin, H., Allerson, C.R., Polycarpou-Schwarz, M., Rofts, A., Rogers, J.T., Kishi, F., Hentze, M.W., Rouault, T.A., Andrews, N.C., and Hediger, M.A. (2001). Iron-dependent regulation of the divalent metal ion transporter. FEBS Lett. *509*, 309–316.

Gunshin, H., Fujiwara, Y., Custodio, A.O., Direnzo, C., Robine, S., and Andrews, N.C. (2005). Slc11a2 is required for intestinal iron absorption and erythropoiesis but dispensable in placenta and liver. J. Clin. Invest. *115*, 1258–1266.

Hubert, N., and Hentze, M.W. (2002). Previously uncharacterized isoforms of divalent metal transporter (DMT)-1: implications for regulation and cellular function. Proc. Natl. Acad. Sci. USA *99*, 12345–12350.

Humphrey, W., Dalke, A., and Schulten, K. (1996). VMD: visual molecular dynamics. J. Mol. Graph. *14*, 33–38, 27–38.

Iolascon, A., and De Falco, L. (2009). Mutations in the gene encoding DMT1: clinical presentation and treatment. Semin. Hematol. *46*, 358–370.

Jardetzky, O. (1966). Simple allosteric model for membrane pumps. Nature *211*, 969–970.

Jiang, W., Phillips, J.C., Huang, L., Fajer, M., Meng, Y., Gumbart, J.C., Luo, Y., Schulten, K., and Roux, B. (2014). Generalized scalable multiple copy algorithms for molecular dynamics simulations in NAMD. Comput. Phys. Commun. *185*, 908–916.

Kaback, H.R., Dunten, R., Frillingos, S., Venkatesan, P., Kwaw, I., Zhang, W., and Ermolova, N. (2007). Site-directed alkylation and the alternating access model for LacY. Proc. Natl. Acad. Sci. USA *104*, 491–494.

Karlin, A., and Akabas, M.H. (1998). Substituted-cysteine accessibility method. Methods Enzymol. *293*, 123–145.

Kazmier, K., Sharma, S., Islam, S.M., Roux, B., and McHaourab, H.S. (2014a). Conformational cycle and ion-coupling mechanism of the Na+/hydantoin transporter Mhp1. Proc. Natl. Acad. Sci. USA *111*, 14752–14757.

Kazmier, K., Sharma, S., Quick, M., Islam, S.M., Roux, B., Weinstein, H., Javitch, J.A., and McHaourab, H.S. (2014b). Conformational dynamics of ligand-dependent alternating access in LeuT. Nat. Struct. Mol. Biol. *21*, 472–479.

Krishnamurthy, H., and Gouaux, E. (2012). X-ray structures of LeuT in substrate-free outward-open and apo inward-open states. Nature *481*, 469–474.

Li, Q., Wanderling, S., Paduch, M., Medovoy, D., Singharoy, A., McGreevy, R., Villalba-Galea, C.A., Hulse, R.E., Roux, B., Schulten, K., et al. (2014). Structural mechanism of voltage-dependent gating in an isolated voltage-sensing domain. Nat. Struct. Mol. Biol. *21*, 244–252.

Lieu, P.T., Heiskala, M., Peterson, P.A., and Yang, Y. (2001). The roles of iron in health and disease. Mol. Aspects Med. *22*, 1–87.

Mackenzie, B., and Hediger, M.A. (2004). SLC11 family of H+-coupled metal-ion transporters NRAMP1 and DMT1. Pflugers Arch. *447*, 571–579.

Mackenzie, B., Takanaga, H., Hubert, N., Rolfs, A., and Hediger, M.A. (2007). Functional properties of multiple isoforms of human divalent metal-ion transporter 1 (DMT1). Biochem. J. *403*, 59–69.

Malinauskaite, L., Quick, M., Reinhard, L., Lyons, J.A., Yano, H., Javitch, J.A., and Nissen, P. (2014). A mechanism for intracellular release of Na+ by neurotransmitter/sodium symporters. Nat. Struct. Mol. Biol. *21*, 1006–1012.

McCoy, A.J., Grosse-Kunstleve, R.W., Adams, P.D., Winn, M.D., Storoni, L.C., and Read, R.J. (2007). Phaser crystallographic software. J. Appl. Crystallogr. *40*, 658–674.

McGreevy, R., Singharoy, A., Li, Q., Zhang, J., Xu, D., Perozo, E., and Schulten, K. (2014). xMDFF: molecular dynamics flexible fitting of low-resolution X-ray structures. Acta Crystallogr. D Biol. Crystallogr. *70*, 2344–2355.

McGreevy, R., Teo, I., Singharoy, A., and Schulten, K. (2016). Advances in the molecular dynamics flexible fitting method for cryo-EM modeling. Methods *100*, 50–60.

Otwinowski, Z., and Minor, W. (1997). Processing of X-Ray Diffraction Data Collected in Oscillation Mode. (Elsevier), pp. 307–326.

Penmatsa, A., and Gouaux, E. (2014). How LeuT shapes our understanding of the mechanisms of sodium-coupled neurotransmitter transporters. J. Physiol. *592*, 863–869.

Perez, C., Koshy, C., Yildiz, O., and Ziegler, C. (2012). Alternating-access mechanism in conformationally asymmetric trimers of the betaine transporter BetP. Nature *490*, 126–130.

Pottier, M., Oomen, R., Picco, C., Giraudat, J., Scholz-Starke, J., Richaud, P., Carpaneto, A., and Thomine, S. (2015). Identification of mutations allowing natural resistance associated macrophage proteins (NRAMP) to discriminate against cadmium. Plant J. *83*, 625–637.

Shawki, A., Knight, P.B., Maliken, B.D., Niespodzany, E.J., and Mackenzie, B. (2012). H(+)-coupled divalent metal-ion transporter-1: functional properties, physiological roles and therapeutics. Curr. Top Membr. *70*, 169–214.

Shi, Y. (2013). Common folds and transport mechanisms of secondary active transporters. Annu. Rev. Biophys. *42*, 51–72.

Shimamura, T., Weyand, S., Beckstein, O., Rutherford, N.G., Hadden, J.M., Sharples, D., Sansom, M.S., Iwata, S., Henderson, P.J., and Cameron, A.D. (2010). Molecular basis of alternating access membrane transport by the sodium-hydantoin transporter Mhp1. Science *328*, 470–473.

Singharoy, A., Venkatakrishnan, B., Liu, Y., Mayne, C.G., Lee, S., Chen, C.H., Zlotnick, A., Schulten, K., and Flood, A.H. (2015). Macromolecular crystallography for synthetic abiological molecules: combining xMDFF and PHENIX for structure determination of cyanostar macrocycles. J. Am. Chem. Soc. *137*, 8810–8818.

Soe-Lin, S., Apte, S.S., Andriopoulos, B., Jr., Andrews, M.C., Schranzhofer, M., Kahawita, T., Garcia-Santos, D., and Ponka, P. (2009). Nramp1 promotes efficient macrophage recycling of iron following erythrophagocytosis in vivo. Proc. Natl. Acad. Sci. USA *106*, 5960–5965.

Su, M.A., Trenor, C.C., Fleming, J.C., Fleming, M.D., and Andrews, N.C. (1998). The G185R mutation disrupts function of the iron transporter Nramp2. Blood *92*, 2157–2163.

Tavoulari, S., Margheritis, E., Nagarajan, A., DeWitt, D.C., Zhang, Y.W., Rosado, E., Ravera, S., Rhoades, E., Forrest, L.R., and Rudnick, G. (2016). Two Na+ sites control conformational change in a neurotransmitter transporter homolog. J. Biol. Chem. *291*, 1456–1471.

Tetsch, L., Koller, C., Donhofer, A., and Jung, K. (2011). Detection and function of an intramolecular disulfide bond in the pH-responsive CadC of *Escherichia coli*. BMC Microbiol. *11*, 74.

Touret, N., Martin-Orozco, N., Paroutis, P., Furuya, W., Lam-Yuk-Tseung, S., Forbes, J., Gros, P., and Grinstein, S. (2004). Molecular and cellular mechanisms underlying iron transport deficiency in microcytic anemia. Blood *104*, 1526–1533.

Verma, R. (2000). PCR of the v region. Methods Mol. Med. *40*, 453–459.

Veuthey, T., and Wessling-Resnick, M. (2014). Pathophysiology of the Belgrade rat. Front Pharmacol. *5*, 82.

Watanabe, A., Choe, S., Chaptal, V., Rosenberg, J.M., Wright, E.M., Grabe, M., and Abramson, J. (2010). The mechanism of sodium and substrate release from the binding pocket of vSGLT. Nature *468*, 988–991.

Xu, H., Jin, J., DeFelice, L.J., Andrews, N.C., and Clapham, D.E. (2004). A spontaneous, recurrent mutation in divalent metal transporter-1 exposes a calcium entry pathway. PLoS Biol. *2*, E50.

Yamashita, A., Singh, S.K., Kawate, T., Jin, Y., and Gouaux, E. (2005). Crystal structure of a bacterial homologue of Na+/Cl-dependent neurotransmitter transporters. Nature *437*, 215–223.

Yokoyama, W.M. (2008). Production of monoclonal antibody supernatant and ascites fluid. Curr. Protoc. Mol. Biol. *Chapter 11*, Unit 11.10.

Zhao, Y., Terry, D.S., Shi, L., Quick, M., Weinstein, H., Blanchard, S.C., and Javitch, J.A. (2011). Substrate-modulated gating dynamics in a Na+-coupled neurotransmitter transporter homologue. Nature *474*, 109–113.

Structure, Volume *24*

Supplemental Information

Crystal Structure and Conformational Change Mechanism of a Bacterial Nramp-Family Divalent Metal Transporter

Aaron T. Bozzi, Lukas B. Bane, Wilhelm A. Weihofen, Abhishek Singharoy, Eduardo R. Guillen, Hidde L. Ploegh, Klaus Schulten, and Rachelle Gaudet

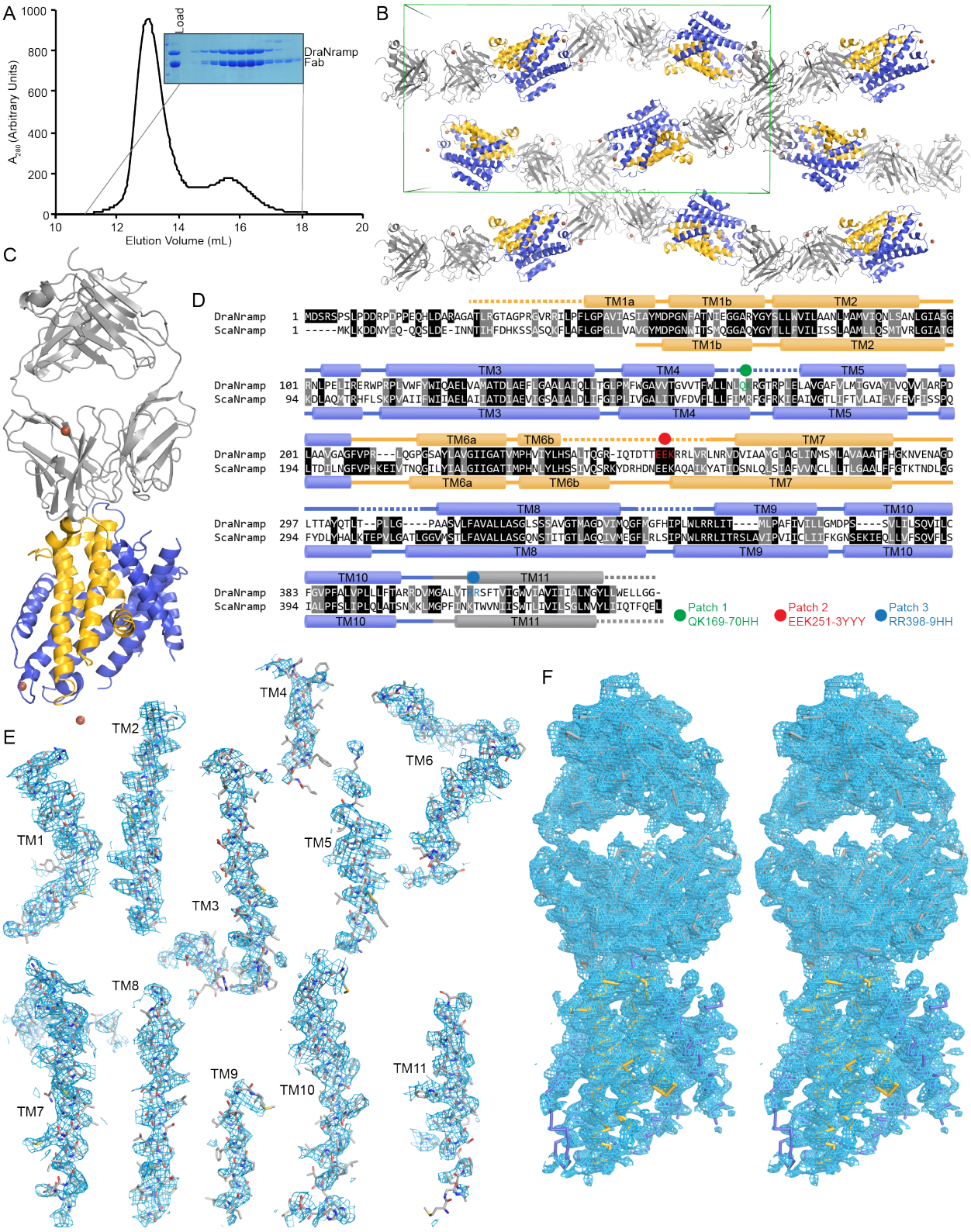

Figure S1, related to Figure 1. Crystal structure of DraNramp bound to a Fab. (A) SEC trace of 1:1.2 DraNramp-Fab mixture, and Coomassie-stained SDS-PAGE of the resulting fractions. (B) Crystal packing of DraNramp-Fab crystals. The Fab variable regions primarily bind extracellular loop 7-8, and crystal packing interactions involve Fab-Fab interfaces as well as an interaction between the Fab constant regions and DraNramp intracellular loops.

Unit cell is shown in green for scaling reference. (C) The asymmetric unit contains one DraNramp transporter (blue and yellow), one Fab (gray), and three osmium ions (ruby). (D) Sequence alignment of *Deinococcus radiodurans* (DraNramp) and *Staphylococcus capitis* (ScaNramp), with their secondary structure indicated above or below the sequence, respectively. The overall sequence identity is 38%. (E) Final $2F_o$-F_c electron density map contoured at 1σ and corresponding model in sticks representation for each transmembrane segment of DraNramp. (F) Stereo image of the final $2F_o$-F_c electron density map contoured at 1σ. In all panels except (E), the bundle (TM1, 2, 6, 7) is colored yellow and the scaffold is colored blue.

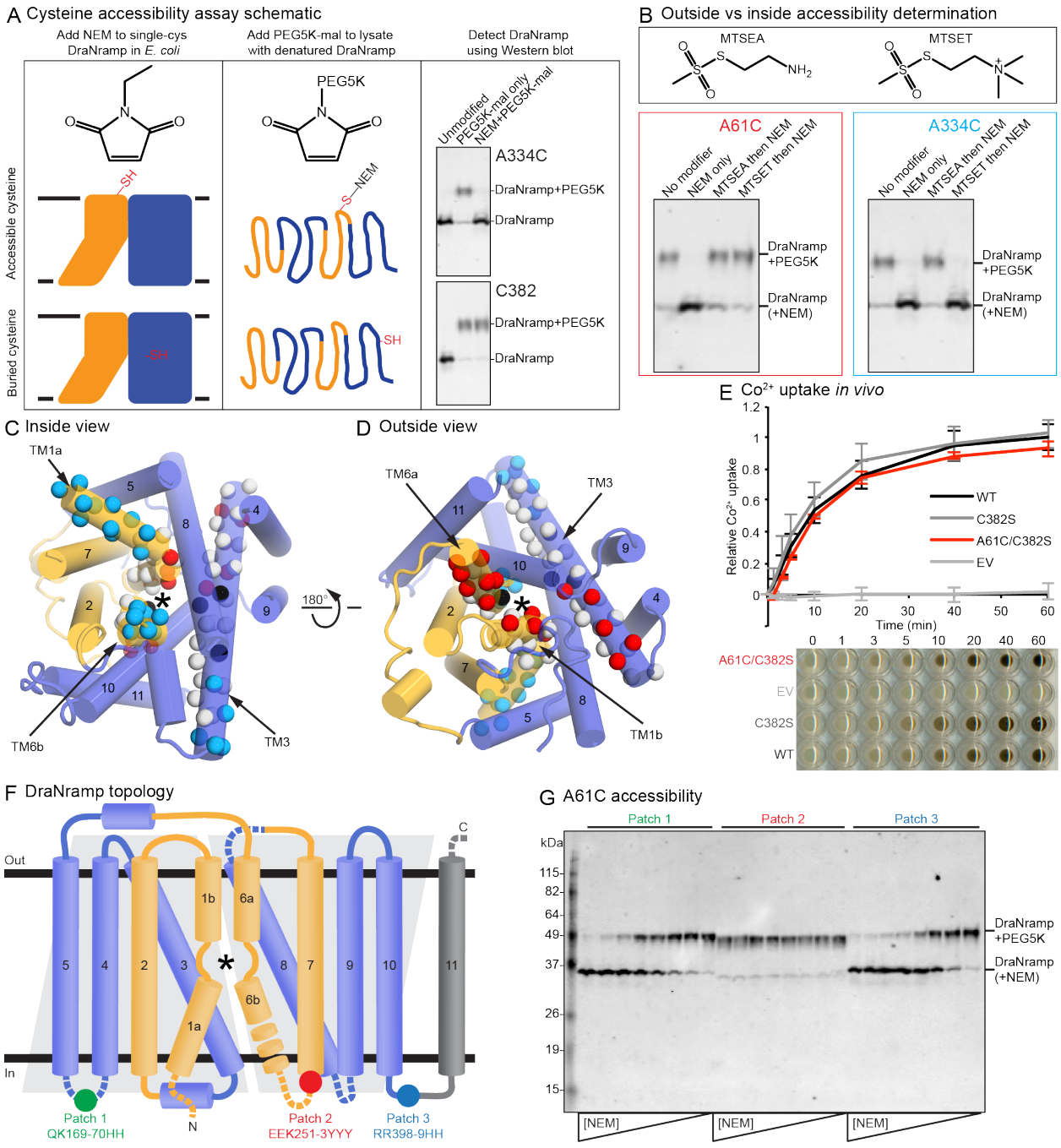

Figure S2, related to Figure 2. Cysteine accessibility and cobalt transport assays reveal location of outward metal permeation pathway. (A) For our *in vivo* cysteine accessibility assay, we added NEM to a panel of ~100 single-cysteine DraNramp mutants. Accessible cysteines (e.g. A334C) in the native protein react irreversibly with NEM, whereas buried cysteines (e.g. C382) do not. We then lyse the cells and denature the proteins in urea, sodium dodecyl sulfate, and dithiothreitol and add a maleimide derivative conjugated to PEG5K, which reacts with previously unmodified cysteines. We then use a Western blot for the N-terminal His-tag to observe a gel shift as a result of the PEG5K addition, which is prevented by reaction with NEM in the first step. By comparing the intensities of the lower and upper bands in the control case (PEG5K only) with their intensities when both NEM and PEG5K were added, we can determine the NEM-modified protein fraction. (B) The inner-membrane impermeable MTSET reagent allows us to determine whether accessible cysteines are modified from the cytosol or the periplasm. We add either MTSET or the similar but membrane-permeable MTSEA before adding NEM (thus blocking NEM

modification). However, these reagents form reversible disulfides that are cleaved by DTT in the denaturation step, thus allowing PEG5K-maleimide to react and observation of the upper band on the Western blot. For an outward-accessible position like A61C, both MTSEA and MTSET block NEM modification, whereas for an inward-accessible position like A334C, only MTSEA blocks NEM modification. (C,D) Cysteine-accessibility data from Table S1 plotted onto the DraNramp structure. View from the cytosol (C) showing the large cavity with inward-accessible positions (cyan spheres) that line the path to the metal-binding site (*).View from the periplasm (D) showing the outward-accessible positions (red spheres) that line the proposed metal permeation pathway to the binding site (*) in the alternate outward-open conformation. Black spheres were only accessible to NEM, and gray spheres were inaccessible to all modifiers. (E) *In vivo* Co^{2+} uptake assay allows comparison of the metal transport function of DraNramp mutants by measuring the pellet darkness (due to accumulated Co^{2+} precipitated as black solid CoS at the end of the assay). The A61C/C382S single-cysteine reporter mutant retains full activity. Data are averages ± s.d. ($n \geq 3$). (F) The three patch mutants made to our crystallization construct are located in the intracellular loops 4-5 (QK169-170HH), 6-7 (EEK251-253YYY), and 10-11 (RR398-399HH). The inverted repeat topology is indicated with light gray trapezoids, with the bundle and scaffold colored yellow and blue, respectively. The metal-binding site is marked (*), and loops disordered in the DraNramp structure are dashed. (G) We can assess the effect of mutations (such as the crystallization construct patch mutants) on NEM-modification of the A61C single-cysteine reporter across an NEM concentration gradient. For patch mutants 1 and 3, NEM modification reached completion at high NEM concentrations (complete elimination of the upper PEG5K band), with a slightly higher NEM concentration at midpoint for patch 1. For patch mutant 2, the lack of NEM modification at any tested concentration indicates this mutation causes A61C to be fully protected (buried), likely by locking the protein in the observed inward-facing conformation. A61C fractional modification data extracted from this Western blot are included in Figure 2D.

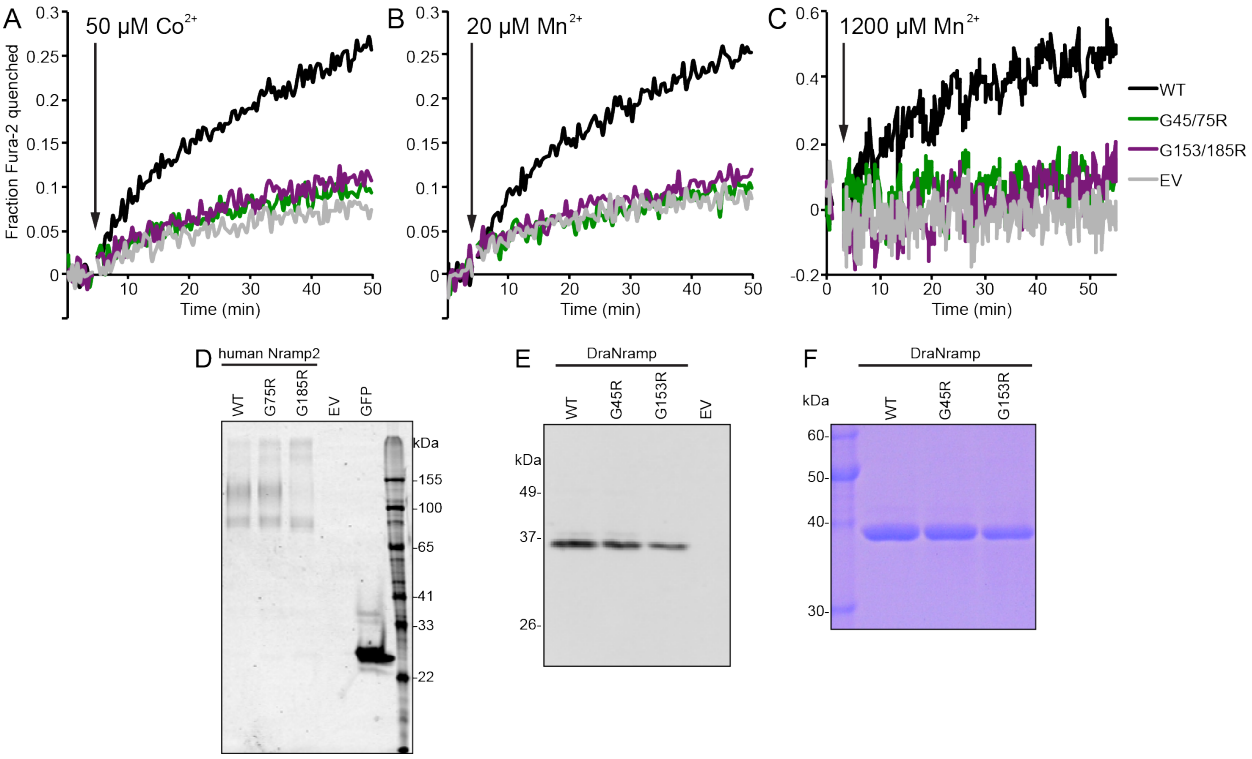

Figure S3, related to Figure 3. Loss of function glycine-to-arginine mutants are expressed for both human Nramp2 and DraNramp. (A-B) Transport of the transition metals Co^{2+} (A) and Mn^{2+} (B) in transfected HEK cells was monitored as quenching of Fura-2 fluorescence. Both G-to-R mutants exhibited severe loss of function (no transport activity above baseline) compared to WT human Nramp2 for both metals. Traces are representative of at least two independent transfection experiments. (C) We observed significant impairment of Mn^{2+} transport, monitored as quenching of Fura-2 fluorescence, with both G-to-R DraNramp mutants compared to WT when reconstituted into proteoliposomes. Traces are representative of three experiments. EV = empty vector/vesicle. (D) In-gel GFP fluorescence image of SDS-PAGE gel showing that C-terminally GFP-tagged G-to-R mutants both expressed in transfected HEK cells, although G185R expressed somewhat less. (E) Western blot, using an anti-His-tag antibody, showing that G-to-R DraNramp mutants both expressed although G153R expressed somewhat less. (F) Coomassie-stained SDS-PAGE gel of purified protein samples showing that both G-to-R DraNramp could readily be purified from *E. coli* membranes.

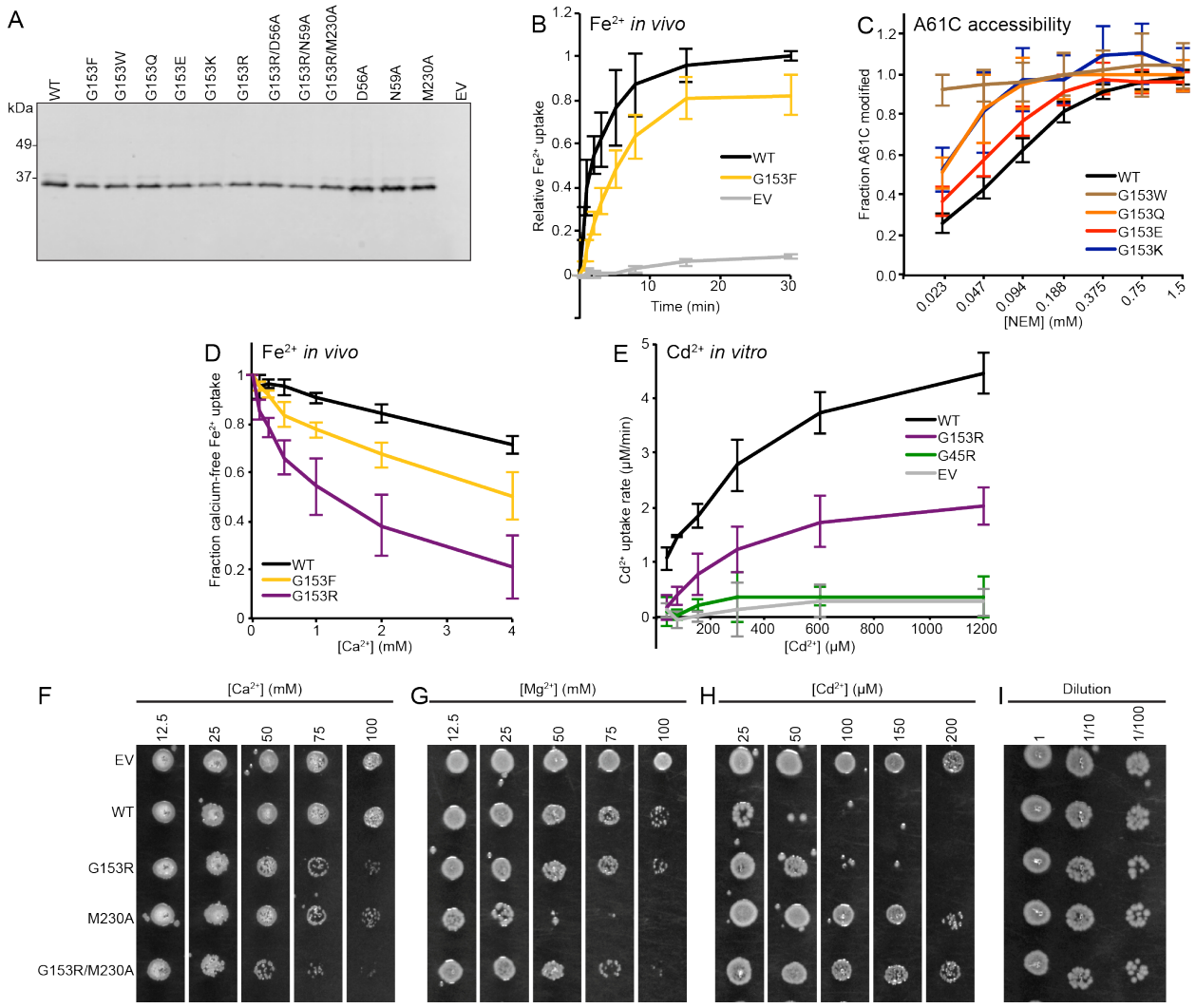

Figure S4, related to Figure 4. G153 mutations in DraNramp perturb outward-facing conformation and alter metal selectivity. (A) Western blot showing G153X mutants all expressed, but slightly less than WT. (B) G153F mutant exhibits slightly reduced *in vivo* Fe^{2+} transport. (C) All tested bulky substitutions at G153 increase the NEM-labeling rate of the A61C single-cysteine reporter, with G153F and G153W having the most dramatic effects. (D) Ca^{2+} competition reduces *in vivo* Fe^{2+} transport (15 min uptake in DraNramp-expressing *E. coli*) to a lesser degree for G153F than G153R, suggesting that the arginine perturbs the binding site in a manner particularly favorable to Ca^{2+}. WT and G153R data are reproduced from Figure 4E. (E) G153R impaired Cd^{2+} transport over a range of concentrations in an *in vitro* proteoliposome assay. Data are averages ± s.d. ($n \geq 3$). (F-I) Metal toxicity assessed using growth of DraNramp-expressing *E. coli* on LB-agar plates containing indicated metal concentrations (EV is empty vector control). (F) G153R increased sensitivity to Ca^{2+}, and G153R/M230A further increased sensitivity, suggesting synergistic perturbations to favor Ca^{2+} transport. (G) G153R did not increase Mg^{2+} toxicity, and G153R/M230A increased tolerance compared to M230A, suggesting that the G153R perturbation could be somewhat Ca^{2+} specific. (H) G153R enhanced Cd^{2+} tolerance less so than M230A. (I) Control serial dilutions on plates with no metal added. The gamma values were adjusted in the same manner for each condition to increase contrast between bacterial colonies and background. Growth trends are representative of three experiments.

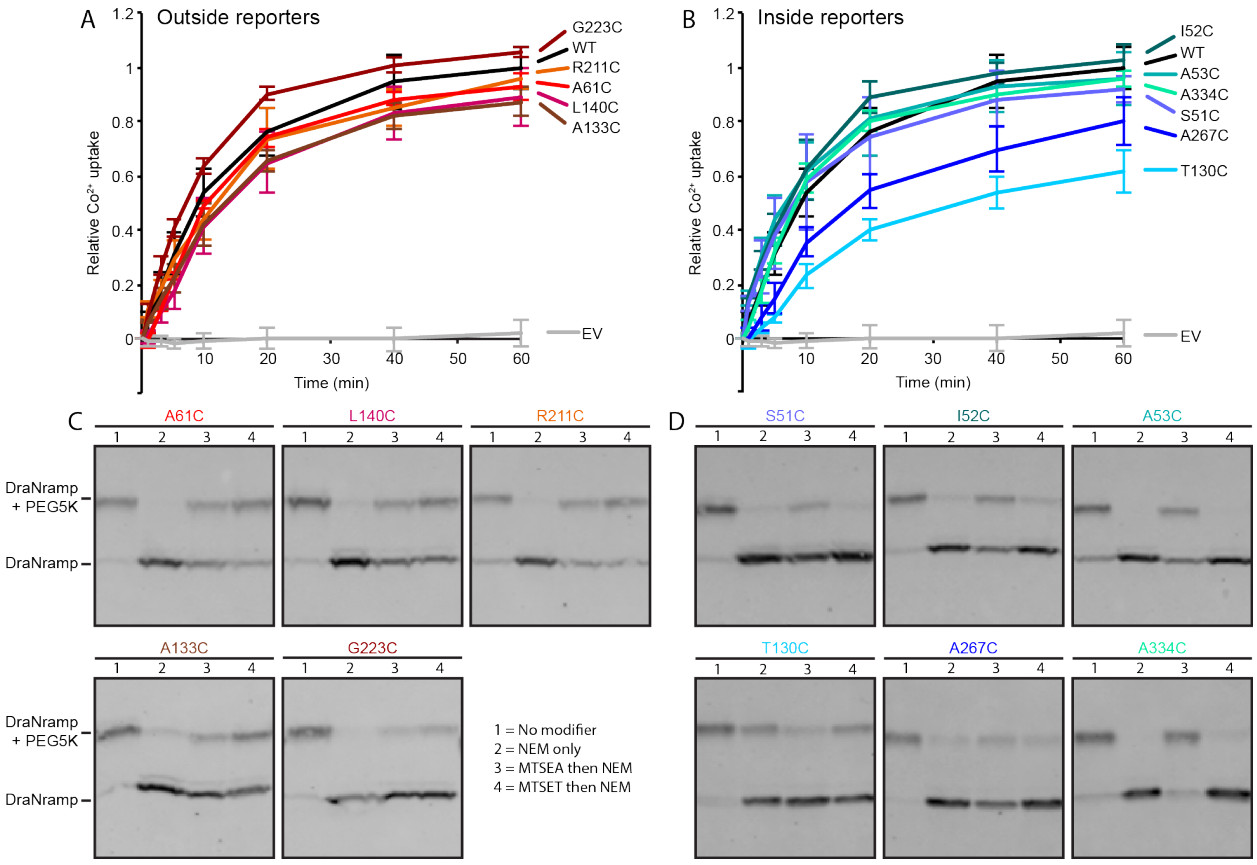

Figure S5, related to Figure 6. Inside and outside-accessible single-cysteine reporters preserve metal transport function. (A,B) *In vivo* Co^{2+} transport of outside (A) and inside (B) single-cysteine reporters. All mutants demonstrated significant activity, with only T130C and A267C showing some decrease below WT level. Data are averages ± s.d. ($n \geq 3$). (C,D) Solvent accessibility of outside (C) and inside (D) single-cysteine reporters using the membrane-impermeable cysteine modifier MTSET and the similar but membrane-permeable MTSEA, as described in Figure S2.

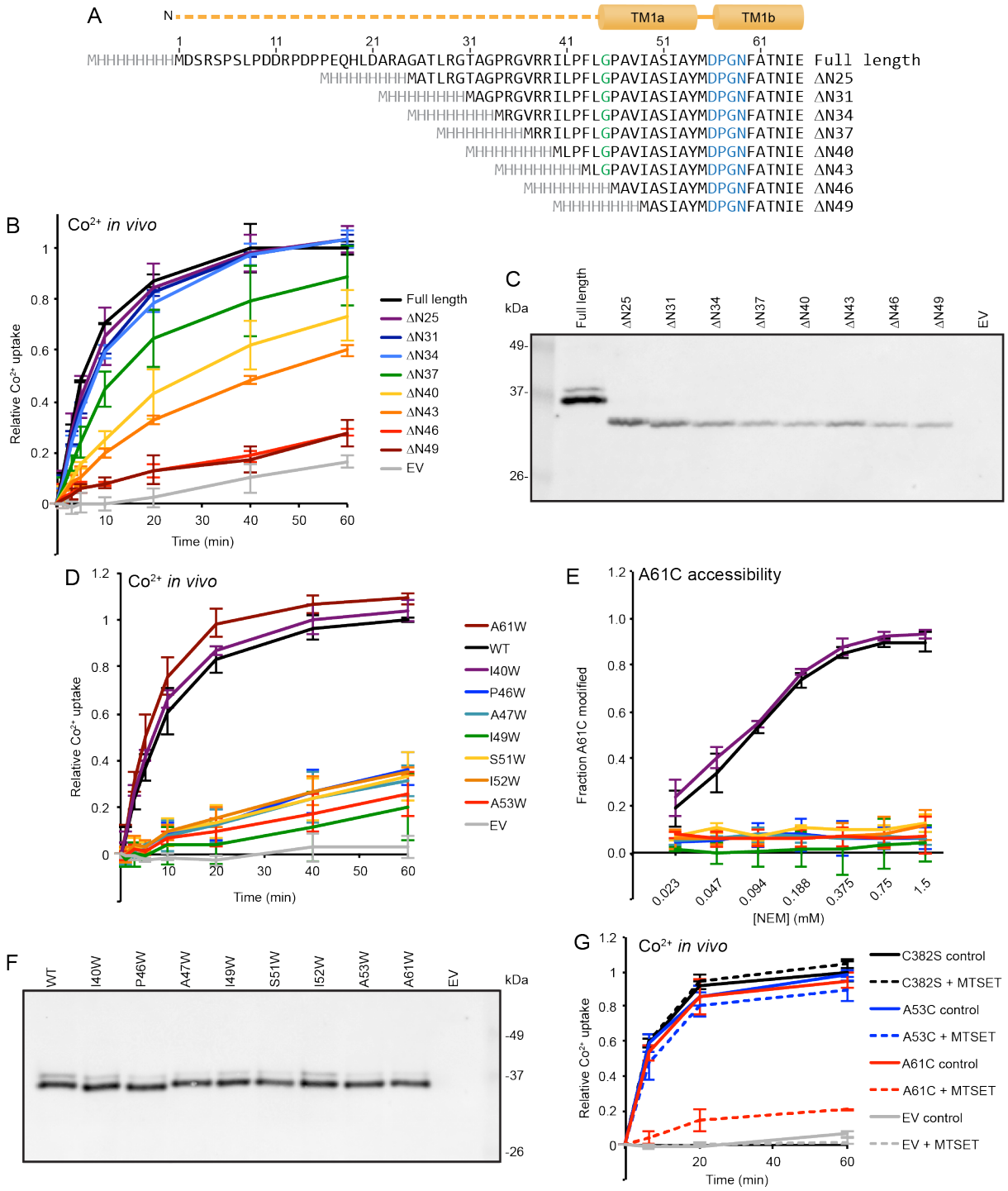

Figure S6, related to Figure 7. TM1a modification impairs DraNramp metal transport. (A) A series of N-terminal truncations removed from 25 to 49 residues while retaining the N-terminal 8His-tag (MHHHHHHHHH). (B) While ΔN25, ΔN31, and ΔN34 retained Co^{2+} uptake activity similar to full length DraNramp, ΔN37, ΔN40, and ΔN43 showed a gradual decrease in activity. ΔN46 and ΔN49, which both cut into TM1a, showed a severe loss of transport activity. Data are averages ± s.d. (n = 3). (C) Expression is reduced for N-terminal truncations compared to the full-length DraNramp as determined using a Western blot against the N-terminal His-tag. However, expression was similar for ΔN34 through ΔN49, although there were pronounced differences in transport activity. (D) Inserting tryptophans in place of residues P46, A47, I49, S51, I52, or A53 on TM1a inhibits Co^{2+} transport, while I40W

(preceding TM1a) does not. Interestingly, the TM1b A61W mutant retains full metal transport activity, consistent with the lack of impairment observed with NEM modification of A61C in Figure 7A, demonstrating that steric bulk can be accommodated in this position without impairing function. Data are averages ± s.d. (n = 3). (E) The six tested TM1a tryptophan mutations fully protected the A61C reporter from NEM modification, indicating that the proteins are locked in an inward-open state. The transport-capable I40W mutant showed WT-like A61C labeling. Data are averages ± s.d. (n = 4). (F) Western blot showing that all tested tryptophan mutants express similarly to WT DraNramp. (G) Pretreatment of A61C with the membrane impermeable, positively charged MTSET fully inhibits DraNramp Co^{2+} transport. The cysteine-less C382S and cytoplasmically-oriented A53C (and thus MTSET-inaccessible; Figure S5D) constructs are not significantly affected by MTSET pretreatment. Data are averages ± s.d. (n = 3).

Table S1, related to Figure 2. Cysteine accessibility results plotted on Figures 2A, S2C, and S2D

TM1			TM3			TM6		
Residue	Accessibility	Direction	Residue	Accessibility	Direction	Residue	Accessibility	Direction
E65	0.83	Outward	T146	0.48	--	S217	0.94	Outward
I64	0.35	--	L145	0.37	--	A218	0.94	Outward
N63	0.02	--	L144	0.85	Outward	Y219	0.89	Outward
T62	0.24	--	Q143	0.85	Outward	L220	0.90	Outward
A61	0.88	Outward	I142	0.12	--	A221	0.65	Outward
F60	0.10	--	A141	0.16	--	V222	0.09	--
N59	0.21	--	L140	0.90	Outward	G223	0.98	Outward
G58	0.87	Outward	A139	0.11	--	I224	0.75	Outward
P57	0.13	--	A138	0.12	--	I225	0.10	--
D56	0.92	Outward	G137	0.25	--	G226	0.06	--
M55	0.15	--	L136	0.80	Outward	A227	0.54	N.D.
Y54	0.36	--	F135	0.06	--	T228	0.14	--
A53	0.84	Inward	E134	0.18	--	V229	0.24	--
I52	0.82	Inward	A133	0.91	Outward	M230	0.95	Inward
S51	0.93	Inward	L132	0.15	--	P231	1.00	Inward
A50	0.99	Inward	D131	0.91	N.D.	H232	0.96	Inward
I49	0.91	Inward	T130	0.87	N.D.	V233	0.92	Inward
V48	0.94	Inward	A129	0.17	--	I234	0.95	Inward
A47	0.91	Inward	M128	0.25	--	Y235	0.98	Inward
P46	0.89	Inward	A127	0.19	--	L236	0.96	Inward
G45	0.75	Inward	V126	0.17	--	H237	0.95	Inward
L44	0.90	Inward	L125	0.20	--	S238	0.85	Inward
F43	0.74	Inward	E124	0.51	N.D.	A239	0.90	Inward
P42	0.84	Inward	A123	0.25	--	L240	0.90	Inward
L41	0.88	Inward	Q122	0.16	--	T241	0.75	Inward
I40	0.92	Inward	I121	0.25	--	Q242	0.80	Inward
			W120	0.76	Inward			
			Y119	0.12	--			
			F118	0.20	--			
			W117	0.92	Inward			
			V116	0.25	--			
			L115	0.75	Inward			
			P114	0.84	Inward			
			R113	0.94	Inward			

Supplemental Experimental Procedures

Cell-based metal uptake assays

E. coli cells expressing DraNramp (or an empty vector) were aliquoted 190 µL per well into 96-well round bottom plates at a density of OD_{600} = 5.26 in cobalt assay buffer (50 mM HEPES pH 7.3, 60 mM NaCl, 10 mM KCl, 0.5 mM $MgCl_2$, 0.217 % glucose). Transport was initiated by adding 10 µL of 4 mM $Co(NO_3)_2$ or freshly made 4 mM $FeSO_4$ + 4 mM ascorbic acid. For Ca^{2+} competition experiments, 10 µL of 20X concentrated $CaCl_2$ was added 1 min before Fe^{2+}. For NEM and MTSET pre-modification comparison experiments, cells were incubated with 3 mM NEM for 15 min at RT before cysteine quench or 3 mM MTSET for 30 min at 37°C and then washed twice. After the desired metal uptake time, excess EDTA was added to quench uptake and cells were washed thrice before adding 1% $(NH_4)_2S$ to precipitate internalized Co^{2+} or Fe^{2+}. Cells were pelleted, the supernatant was removed, the plates were scanned, and ImageJ64 was used to quantify the pellet darkness. End point (no metal-subtracted) darkness for WT DraNramp was set as 100% to determine relative transport abilities.

HEK293 cells were transfected with pCDNA3 containing human Nramp2 (with or without a C-terminal GFP tag) using Lipofectamine 2000 (Thermo Fisher) and incubated for 2 days at 30°C. Cells were loaded with Fura-2 AM and washed. A baseline fluorescence measurement (λ_{ex} = 380 nm; λ_{em}=510) was measured for ~3 min with 50 µL of pH 5.5 MES buffer, and then 25 µL of 3X metal was added to give final concentrations of 50 µM $Co(NO_3)_2$, 20 µM $FeSO_4$ + 20 µM ascorbic acid, 20 µM $MnCl_2$, or 20 µM $CdCl_2$ and fluorescence was measured for an additional 45 min. The fraction of the baseline fluorescence quenched was calculated for each timepoint, and for each mutant wells with similar baseline fluorescence values were used to generate the representative traces for each metal.

In vitro metal transport

Purified DraNramp was reconstituted into liposomes made from POPE, POPC, and POPG (Avanti Polar Lipids) in a 50:35:15 ratio by mixing 1:500 protein:lipid in a 5 mM DM solution and dialyzing for 3-4 days in 10 mM MOPS pH 7, 100 mM KCl. Liposomes were permeabilized using freeze-thaw cycles to load 100 µM Fura-2, extruded 21 times through a 400 nm filter, and separated from external dye using a PD10 column. Liposomes were diluted three-fold into 10 mM MOPS pH 7, 100 mM NaCl and baseline fluorescence measured, after which 50 nM valinomycin was added to establish a negative internal potential along with metal substrate ($CdCl_2$, $MnCl_2$, or $CaCl_2$). Fluorescence (l_{ex}=340 and 380 nm; l_{em}=510 nm) was monitored at RT for 45 min, before adding 0.25 µM ionomycin at 60 min to measure maximum signal. The intraliposome concentration of Cd^{2+} or Ca^{2+} was determined using: $[M^{2+}]_{inside} = ([M^{2+}]_{free}[Fura\text{-}2]_{total})/(K_D + [M^{2+}]_{free}) + [M^{2+}]_{free}$, where K_D is the K_D of the M^{2+} and Fura-2 (Cd^{2+} = 1 pM; Ca^{2+} = 135 nM) (Grynkiewicz et al., 1985; Hinkle et al., 1992) while relative fluorescence quenching (with post-ionomycin set to 100%) was determined for Mn^{2+}. Transport rates were determined by linear regression of the data for the first 5 min after Cd^{2+} addition and the first 30 min after Ca^{2+} addition.

Toxicity assay

Plates containing indicated concentrations of added $MgCl_2$, $CaCl_2$, or $CdCl_2$ were prepared by mixing 4 mL 10X metal with 36 mL LB-ampicillin-agar. Cells (1 µL at OD600=0.01 and additional serial dilutions on control plate) were plated 90 min post-induction and incubated overnight at 37°C. Plates were imaged on an AlphaImager system and gamma values were adjusted the same way for all images to increase contrast between colonies and the background agar.

Supplemental References

Grynkiewicz, G., Poenie, M., and Tsien, R.Y. (1985). A new generation of Ca^{2+} indicators with greatly improved fluorescence properties. J Biol Chem *260*, 3440-3450.

Hinkle, P.M., Shanshala, E.D., 2nd, and Nelson, E.J. (1992). Measurement of intracellular cadmium with fluorescent dyes. Further evidence for the role of calcium channels in cadmium uptake. J Biol Chem *267*, 25553-25559.